Resonant inelastic X-ray scattering

Frank M F de Groot, Maurits W Haverkort, Hebatalla Elnaggar, Amelie Juhin, Ke-Jin Zhou, Pieter Glatzel

Resonant inelastic X-ray scattering

Frank M. F. de Groot [1,2], Maurits W. Haverkort[3], Hebatalla Elnaggar[4], Amélie Juhin[4], Ke-Jin Zhou[1], Pieter Glatzel[5]

[1]Diamond Light Source, Harwell Campus, Didcot, UK. [2]Debye Institute for Nanomaterials Science, Utrecht University, Utrecht, the Netherlands. [3]Heidelberg University, Heidelberg, Germany. [4]Institute of Mineralogy, Physics of Materials and Cosmochemistry, CNRS, Sorbonne University, Paris, France. [5]European Synchrotron Radiation Facility, Grenoble, France. ✉ e-mail: f.m.f.degroot@uu.nl; kejin.zhou@diamond.ac.uk

Abstract

Resonant inelastic X-ray scattering (RIXS) is a powerful technique that combines spectroscopy and inelastic scattering to probe the electronic structure of materials. RIXS is based on the interaction of X-rays with matter in which the dependence on energy, momentum and polarization is introduced. The RIXS spectra can be approximated as a combination of X-ray absorption and X-ray emission. A 2D RIXS plane can be measured as a function of excitation and emission energies. Using RIXS, collective excitations — such as magnons, phonons, plasmons and orbitons — can be probed in quantum materials, for example, cuprates, nickelates and iridates, with complex low-energy physics and exotic phenomena in energy and momentum space. In addition, RIXS with hard X-rays enables detailed experiments under operando conditions. Spectral broadening owing to short core hole lifetime can be reduced to produce X-ray absorption spectra with high resolution. This Primer gives an overview of RIXS experimentation, data analysis and applications, finishing with a look to the future, where new experimental stations at X-ray free electron lasers promise to revolutionize the understanding of femtosecond processes and non-linear interaction of X-ray with matter

Introduction

Resonant inelastic X-ray scattering (RIXS) is an element- and orbital- selective X-ray spectroscopy technique, based on a two-step, two-photon resonant process. It combines X-ray emission spectroscopy (XES) with X-ray absorption spectroscopy (XAS) by measuring the coherent X-ray emission at an incident X-ray photon energy within the near edge X-ray absorption spectrum. In the first step (X-ray absorption), an electron of the absorbing atom is resonantly excited from a core level to an empty state using an incoming pho- ton characterized by its energy ωi, wave vector ki and polarization state εi. The resulting state, called the intermediate state, carries a core hole with a lifetime of a few femtoseconds. In the second step (X-ray emission), the system radiatively decays into a final state in which the core hole is filled by another electron, either a valence electron or a core electron, accompanied by a photon-out emission characterized by its energy ωo, wave vector ko and polarization state εo. In RIXS, the final state is different from the initial ground state, meaning that the final state is also an excited state. The final state energy is usually higher than the ground state energy, but anti-Stokes lines can also be observed1. RIXS is associated with both an energy transfer ωi−ωo and a momentum transfer ki−ko to the probed system. As a result, it is a scattering technique and a probe of dispersing excitations. The polarization of the incoming εi and outgoing εo light and the resonant energy ωi are involved in the RIXS process, making RIXS a simultaneous spectroscopy and scattering technique.

Figure 1 shows the density of states (DOS) of rutile TiO2 (Fig. 1b), as a representative example of a transition metal oxide. Three different XAS processes are shown, the oxygen 1s (Fig. 1c), titanium 1s (Fig. 1d) and titanium 2p (Fig. 1e). XAS spectra can be described as transitions from a core state to an empty state. The oxygen 1s XAS spectrum can be approximated as an electric dipole transition to the empty oxygen p DOS, indicated in grey. The titanium 1s XAS spectrum consists of a main edge, with dipole transitions to the empty p-states, and a pre- edge region, with dipole transitions to p-character of the 3d band. In addition, there are electric quadrupole transitions to the 3d states. Although quadrupole transitions are substantially weaker, they are important for the pre-edge structure and are used in RIXS experiments. The core hole potential

makes these final states appear as excitons, indicated with red sticks in Fig. 1d, and their incident energy is shifted owing to the core hole potential. These excitons relate to the same initial states as the 3d band but in the final state of titanium 1s XAS they appear at a lower energy2. The titanium 2p XAS is dominated by excitonic states from 2p to 3d transitions, followed by a low intensity edge, often not distinguishable from the background.

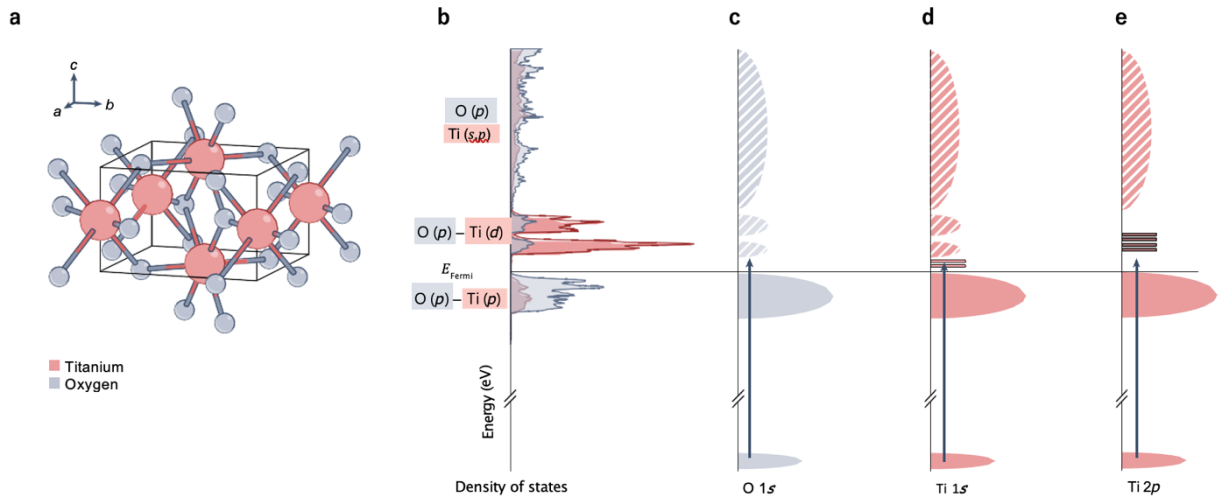

Fig. 1 | Electronic structure of a transition metal oxide. a, Crystal structure of rutile transition metal oxide (TiO_2). **b**, Density of states (DOS) of TiO_2 projected on oxygen (grey) and titanium (red). The Fermi energy is shown as a horizontal solid line. **c**, A schematic of the oxygen 1*s* X-ray absorption (XAS) process, in which an O 1*s* electron is excited to the empty DOS (dashed in the simplified DOS sketch). **d**, Titanium 1*s* XAS process, in which Ti 1*s* electron is excited. **e**, Titanium 2*p* XAS process, in which Ti 2*p* electron is excited to the empty DOS modified by the core hole potential. The solid red horizontal lines represent reachable excitonic states.

An L2,3 edge excitation of 3d transition metal ions creates a 2p core hole, leading to two XAS peaks split by the effect of spin–orbit coupling. The 2p core hole has large two-electron interactions with the partly filled 3d states. These large two-electron integrals, also known as multiplet effects, must be explicitly included in the calculation of the 2p XAS spectral shapes, in which the 2p XAS spectrum can be considered as excitonic3. Figure 2 shows an overview of the RIXS features of a transition metal oxide. Figure 2a shows a one-electron picture of the RIXS pro- cess, also known as a level diagram. In the valence RIXS process, a core electron is excited to a 3d state, which decays back to the core state. In the fluorescence process, a core electron is excited to a free electron state and a valence electron decays back to the core state. Not all RIXS processes can be described in a one-electron model. Figure 2b shows a total energy model of the RIXS process, also known as a state diagram. In a state diagram, the lowest energy state is the ground state. At higher energies, excitations such as phonons and dd excitations occur. The RIXS process can be understood as a transition from the ground state to a core exciton, coupled to the decay of this core exciton back to the ground state or to a low-energy excitation. Fluorescence is easiest to understand from the one-electron picture. In core RIXS, a similar diagram can be drawn.

The resulting 2D RIXS planes at the oxygen 1s (grey) and titanium 1s (red) resonances are shown in Fig. 2c,d, respectively. The oxygen 1s XAS (dashed grey) shows a sharp 3d band and a broad 4s/4p band, both containing oxygen p character. The 2D graph shows the possible RIXS processes close to zero energy loss (thin vertical line). The RIXS plane shows the energy loss (horizontal) of the scattered photons measured as a function of the incident energy (vertical). In the case of oxygen 1s XAS, the RIXS plane (grey) consists of a diagonal band and a vertical band. The diagonal band indicates the non-resonant X-ray emission that appears at constant emission energy. This non-resonant channel can be understood as the combination of the XAS excitation to an empty state coupled to the XES of all occupied states back to the core hole, in which the excited electron does not participate in the decay. The vertical line corresponds to XES back to the electronic ground state with zero or minimal energy loss. The region close to the elastic line contains elementary excitations such as phonons.

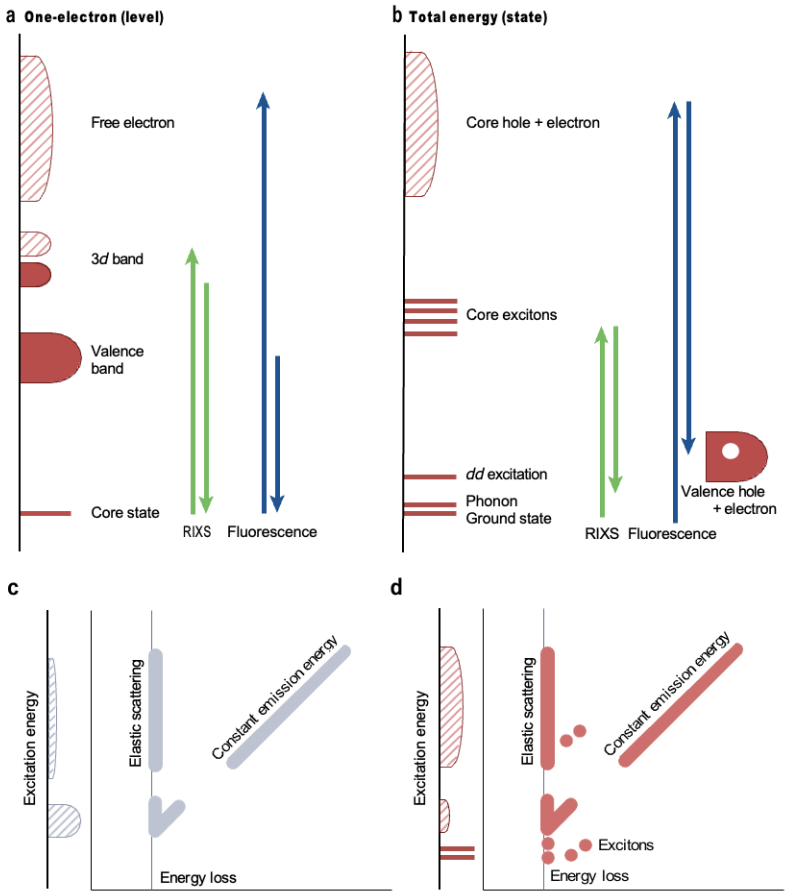

Fig. 2 | Graphical overviews of the resonant inelastic X-ray scattering processes of a transition metal oxide. a, A one-electron (level) model of the resonant inelastic X-ray scattering (RIXS) process. RIXS is indicated with green lines and fluorescence with blue lines. **b**, A many-electron (state) model of the RIXS process, including many-particle core excitons that cannot be described in a one-electron model. **c**, Two-dimensional image of the oxygen 1*s* valence RIXS, in which no excitons are present. The resonant elastic scattering is visible at zero energy loss. **d**, The metal 1*s* valence RIXS, in which there appears additional excitons in the RIXS plane.

In the case of metal 1s XAS (K edge), the RIXS plane (red) contains additional features owing to the excitonic states. Using the 3d7 system CoO as an example, the 1s XAS yields 1s13d8 excitons that decay to 3d7 RIXS final states. These 3d7 final states include the ground state, from elastic scattering, and all excited states of the 3d7 multiplet, referred to as dd excitations. Owing to coupling of the excitons to the band excitations, the dd excitations are also visible at larger excitation energies, where they are referred to as indirect RIXS[4,5]; see Supplementary information for more details. By contrast, in metal 2p XAS, the RIXS plane is dominated by excitons following the transition pathway 3dN > 2p53dN+1 > 3dN. Figure 3 shows the 2p XAS of a Cr3+ impurity in aluminium oxide (Fig. 3c) together with a multiplet simulation of the 3d7 > 2p53d8 transition[6]. Figure 3a shows the corresponding 2p3d RIXS spectra calculated for the pathway 3d7 > 2p53d8 > 3d7, compared with the optical absorption spectrum. The 2p3d RIXS spectra are dominated by dd transitions, some of which are visible in the optical spectrum. Charge-transfer excitations are also visible in more covalent systems. At higher resolutions, low-energy excitations — such as phonons and magnons — can be observed, as indicated in Fig. 3b.

RIXS studies the element-specific excitations of molecules and materials, including vibrations, magnetic excitations, orbital excitations, charge excitations and core excitations. By varying the momentum transfer, phonon, magnon and plasmon dispersions of solids can be measured in energy–momentum space. Working at an absorption edge means that RIXS is element-selective. This is useful when studying a compound with multiple elements. For soft X-ray RIXS, the penetration depth is about hundreds of nanometres, which is ideal for studying thin films and interfaces of epitaxial heterostructures. Highly focused, micron-sized X-ray beams enable analysis of small single crystals that are a bottleneck in neutron scattering. Being a photon-in– photon-out technique, RIXS can determine detailed electronic structures in situ. Active materials, such as batteries and catalysts, can be tracked under working conditions with hard X-ray RIXS to reveal valence, spin and

coordination changes. Examples include quantum materials with unconventional phases and large response functions, such as cuprates, transition metal oxides, iridates or lanthanides; energy materials, including batteries and (electro)catalysts; and metal centres in proteins and related model systems.

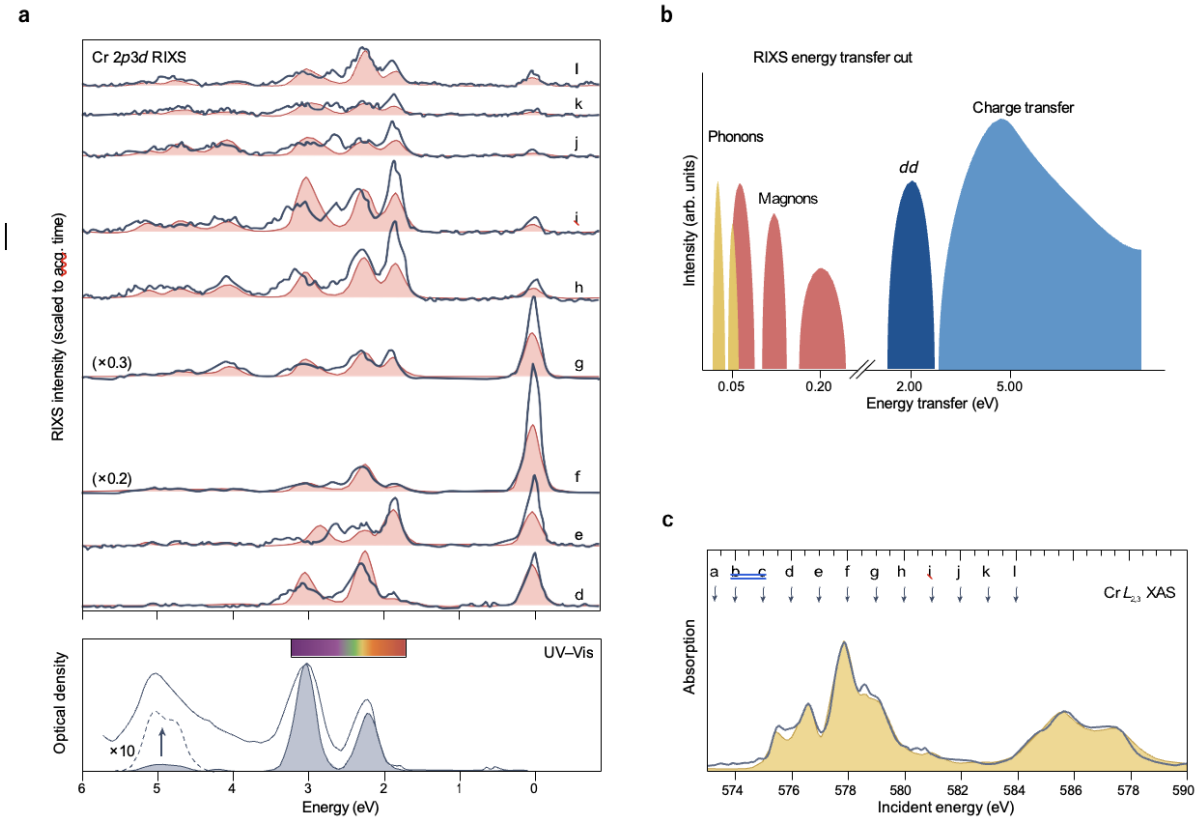

Fig. 3 | Excitations in a 2*p*3*d* resonant inelastic X-ray scattering process. **a**, The 2*p*3*d* resonant inelastic X-ray scattering (RIXS) at the excitation energies as indicated in the X-ray absorption spectroscopy (XAS) spectrum (panel **c**). **b**, Types of excitations in a 2*p*3*d* RIXS experiments. **c**, 2*p* XAS of a Cr^{3+} impurity. UV–Vis, ultraviolet–visible. Panels **a** and **c** adapted with permission from ref. 6, American Chemical Society.

As a photon-hungry technique, RIXS can only be realized at highly brilliant synchrotron radiation sources or free electron lasers (FELs). Typically, at the soft X-ray energy range, RIXS measures the final Typically, at the soft X-ray energy range, RIXS measures the final states following the excitations and de-excitations between transition metal 2p electrons or oxygen 1s electrons and strongly hybrid-ized valence states of 3d transition metal oxides, defined as valence RIXS. Valence RIXS can probe collective excitations and ordering states in quantum materials, such as magnons, phonons and charge density waves (CDWs). Over the past decade, soft X-ray RIXS entered a new era, with dedicated high-resolution facilities constructed at various light sources, reaching an energy resolution of ~20 meV at the copper L edge[7–11]. These new-generation, high-resolution RIXS facilities can probe collective excitations and their interplay in much finer detail and with polarization analysis[12].

RIXS experiments with hard X-rays excite a 1s core electron in 3d systems or a 2p electron in a 4f, 5d or 5f system. X-ray emission is measured with a crystal analyser. Many experiments use a resolution of 0.5–1.0 eV to measure 1s2p or 1s3p RIXS spectra, but some experimental stations can achieve smaller bandwidths down to 20 meV (ref. [13]). These 1s2p or 1s3p RIXS — defined as core RIXS — experiments are ideal to study systems under operando or extreme conditions. Likewise, valence RIXS in the hard X-ray energy range is used for the 2p → 5d → 2p excitation and de-excitation process. High-resolution experiments are important to probe elementary excitations in 4d and 5d transition metal compounds, via the L edges of the transition metal, such as iridates.

Theory

RIXS spectra are given by the double differential cross-section $\frac{\partial^2\sigma}{\partial\Omega\,\partial\omega}$, the fraction of photons scattered in a solid angle Ω and energy window *ω to ω + ∂ω. These are well described by the Kramers–Heisenberg equation14–18:*

$$\frac{\partial^2\sigma}{\partial\Omega\partial\omega} \propto \sum_{\mathrm{f}} \left| \sum_{j} \frac{\langle \mathrm{f}|T^{\dagger}_{\mathbf{k}_\mathrm{o},\boldsymbol{\varepsilon}_\mathrm{o}}|j\rangle\langle j|T_{\mathbf{k}_i,\boldsymbol{\varepsilon}_i}|i\rangle}{\omega_i + E_\mathrm{i} + \mathrm{i}\frac{\Gamma_j}{2} - E_j} \right|^2 \delta(E_\mathrm{i} + \omega_\mathrm{i} - E_f - \omega_\mathrm{o}),$$

in which ω_i is the energy of the incoming light with wave vector $\boldsymbol{k}_\mathrm{i}$ and polarization $\boldsymbol{\varepsilon}_\mathrm{i}$ and ω_o is the energy of the scattered light with wave vector $\boldsymbol{k}_\mathrm{o}$ and polarization $\boldsymbol{\varepsilon}_\mathrm{o}$. E_i is the energy of the initial state and E_f is the energy of the final state. The sum over *j* is a sum over all possible intermediate states with energy E_j (see Supplementary information for more details). The RIXS spectrum is determined by coherent emission ($\langle \mathrm{j}|\, T^{\dagger}_{\boldsymbol{ko},\boldsymbol{\varepsilon o}}\, |\mathrm{i}\rangle$) and absorption ($\langle \mathrm{f}|\, T_{\boldsymbol{ki},\boldsymbol{\varepsilon i}}\, |\mathrm{j}\rangle$) of a photon. As can be seen from the Kramers–Heisenberg equation, the RIXS cross-section depends on the energy *ω*, direction *k* and polarization *ε*. Both the X-ray absorption and X-ray emission operators are dependent on *ω*, *k* and *ε*. The final state is a function of Δ*ω*, Δ*k* and Δ*ε*, from which three important parameters are defined in an RIXS experiment. First, Δ*ω*-RIXS is used to study energy effects, which can be final state core, valence electronic, magnetic or vibrational excitations. Second, Δ*k*-RIXS is used to study momentum-dependent effects, namely, the dispersion of collective excitations such as magnons, phonons and electronic excitations in solids. Finally, Δ*ε*-RIXS is used to study polarization or dichroism effects, which are related to the symmetry properties of the system and can be measured using a linearly or circularly polarized photon-in with polarization analysis of the photon-out. There are not three different modes of RIXS experiments, but Δ*ω*, Δ*k* and Δ*ε* occur in every RIXS experiment

The Kramers–Heisenberg equation contains all the information needed to understand RIXS spectra. Valence RIXS can study the energy momentum dispersion of low-energy excitations such as magnons19–24, spinons25,26, orbitons26–29, phonons30–33, CDWs34–38, mixed modes22,39,40 and multiple excitations of the fundamental excitation modes41–45 (Table 1). In molecules and isolated metal ions, the momentum disper- sion is generally not important and vibrational modes46–48, crystal-field multiplet5 and charge-transfer49 excitations can be observed.

Table 1 | Low-energy excitations in a resonant inelastic X-ray scattering process

Excitation	Optical Raman, IXS and RIXS at *K* edges	RIXS at *L* edges
Lattice	Electron–phonon coupling	None extra
Spin	Bi-magnon (two magnons at different sites)	+1-magnon (direct); +2-magnon (on the same site); +3-magnon (on the same site)
	1-magnon (with large valence spin–orbit)	
	2-spinon (1D spin-1/2 systems)	
Charge	Plasmon Phason mode (charge density wave)	None extra
Orbital	Orbiton (*dd* excitation)	+Spin–orbiton

Excitations related to lattice, spin, charge and orbital excitations. One needs resonant inelastic X-ray scattering (RIXS) at a core level with an orbital moment to allow excitations with a spin change and the last column contains the additional possible transitions. For the spin degree of freedom, spin angular momentum is conserved ($\Delta S_z = 0$) at the metal of oxygen *K* edges; however, it can be changed at the metal *L* edges ($\Delta S_z \neq 0$). IXS, inelastic X-ray scattering.

The relative intensity of a low-energy excitation depends on the resonant energy of the incoming light and the polarization of both incoming and scattered light. In RIXS, the photon generates a core hole, the system time evolves and after some time the core hole is annihilated to produce the scattered photon. During this time, several low-lying excitations — spin, charge, orbital and lattice — can be generated at and around the site where the core hole is created. The presence of a non-dispersive, strongly interacting core hole in the intermediate state has led to reasonably effective theories for describing RIXS spectra as a sum over low-

energy dynamical structure factors[24,50–53]. These theories factorize the momentum dependence in RIXS to a structure factor and atomic scattering length. The former depends on the position of the atoms, and the latter depends on the polarization of the light and reso- nant energy[25,42,54]. For simple models, effective RIXS operators can be compared with numerically exact results[53,55]. For a one-band Hubbard model, exact effective operators can be defined. However, they are not given by a single susceptibility, but by a sum over many possible low- energy excitations. For an extended discussion, see the Supplementary information.

In core RIXS, the momentum dependence of the light is not important as core levels do not disperse. An interesting approach to understand the RIXS spectrum is to approximate it as a convolution of the XAS spectrum with the non-resonant XES spectrum[56]. If this approximation holds — as it does when there is weak interaction of the core hole with the photoexcited electron — all information contained in the constant emission features of an RIXS spectrum will also be in the XAS and non-resonant XES spectra. The only exception is the absolute energy calibration of the energy loss features by elastic scattering, giving the RIXS band gap. The RIXS spectral shape changes depending on the empty DOS probed by the excitation. Measuring a full or partial RIXS plane depends on interference and screening effects, which are system-dependent. The Supplementary information describes how band transitions in the RIXS spectrum can be approximated as the XAS spectrum multiplied with the non-resonant XES spectrum.

Approximated methods for the Kramers–Heisenberg equation can provide additional information to help understand RIXS spectra. Additionally, material-dependent, full theoretical calculations of RIXS spectra are also beneficial. For example, this type of calculation showed that RIXS can be used to measure magnons, long before experiments were possible[57]. Material-specific calculations can either be performed on a model level using material-specific parameters, based on density func- tional theory or on ab initio methods. The boundaries between these different methods are not always clear. Post-Hartree–Fock methods can be used — such as restrictive active space[58], embedded ligand field theory or dynamical mean-field theory[59–61] — either with Hartree–Fock or with density functional theory Kohn–Sham orbitals. Calculating the full RIXS spectrum is usually restricted to relatively small molecules owing to two open shells and charge-transfer excitations in the intermediate state.

Comparison with other techniques

Table 2 compares RIXS with related techniques. RIXS can be described as a combination of XAS and XES. The core resonance adds element specificity, sensitivity to collective excitations and extra polarization options, such as magnetic circular dichroism (MCD). Inelastic X-ray scattering (IXS) is a non-resonant version of RIXS. IXS can measure the momentum transfer of collective excitations[62–64]. It is performed with a hard X-ray energy regime, in which crystal optics achieve a resolution under 1 meV. This energy resolution makes IXS an ideal probe of lowenergy loss charge excitations such as phonons. However, being a non-resonance technique (unlike RIXS), the magnetic scattering cross-section is much smaller than the charge scattering cross-section; hence, magnetic excitations have very low intensity.

The electron analogue of IXS is inelastic electron scattering, which is usually indicated as electron energy loss spectroscopy (EELS). The resolution is ~10 meV and momentum transfer can be measured. EELS can be combined with microscopy using an electron microscope. This gives energy and/or momentum resolution plus spatial resolution[65]. In principle, EELS can be performed at a core resonance, enabling mapping of large momentum transfers. This would complement RIXS offering access to much wider momentum space (Δk). In addition, the information provided would be surface-sensitive.

Raman is the scattering of ultraviolet (UV) and visible light. Optical Raman is analogous to RIXS, in which the small wave vector of UV and visible photons means that no momentum transfer is possible. Raman can be performed at optical resonances, which in this case would be analogous to an RIXS experiment but in the optical regime. Raman experiments can probe low-energy loss excitations such as magnons and phonons at the centre of the Brillouin zone complementing RIXS experiments.

Inelastic neutron scattering (INS) can also produce momentum transfer and energy maps of dipolar magnetic excitation, with superior energy resolution than RIXS66,67. However, INS requires sample quanti- ties on the order of grams, with a large size owing to large penetration depth and unfocused beam. Angle-resolved photoemission spectroscopy is an important technique for band mapping the occupied states and fermionic quasiparticles in the energy–momentum space68–70. By comparison, RIXS maps the neutral electron–hole excitations and bosonic quasiparticles, which are collective excitations.

Table 2 | Comparison of resonant inelastic X-ray scattering with related techniques

Experiment	Abbreviation	Description	Notes
Inelastic X-ray scattering	IXS	Inelastic scattering of X-rays	1 meV, momentum transfer Not resonant
Resonant elastic X-ray scattering	REXS	Resonant elastic X-ray scattering	No energy loss Scattering/diffraction in ordered systems
Resonant inelastic X-ray scattering	RIXS	Combination of X-ray absorption and emission spectroscopy	20 meV Element-specific Sensitive to collective excitations in lattice, charge, orbital and spin degrees of freedom Polarization options (linear and circular dichroism)
Electron energy loss spectroscopy	EELS	Inelastic scattering of electrons	10 meV, momentum transfer Combination with microscopy Resonant EELS
Raman	–	Inelastic scattering of optical/ultraviolet photons	<1 meV, no momentum transfer Resonant Raman
Inelastic neutron scattering	INS	Inelastic scattering of neutrons	<1 meV, momentum transfer Sensitive to magnons
Angle-resolved photoemission spectroscopy	ARPES	X-ray photoemission	<1 meV, momentum transfer Band mapping of occupied states

The best energy resolutions are given in millielectronvolts.

The Experimentation section introduces RIXS beamlines and sample conditions. RIXS experiments are divided into core and valence RIXS. Valence RIXS can measure low-energy excitations, including magnons and phonons, in addition to high-energy electronic excitations, such as charge-transfer and dd excitations. The Results section introduces core RIXS and valence RIXS, with examples provided in the Applications section. The Primer ends with an outlook on potential future developments. Several reviews and books have been written on RIXS17,48,71–82. This Primer complements these works by discussing both theoretical and experimental aspects and recent advances in both soft and hard X-ray ranges, with a focus on applications to solid materials, with molecular systems discussed only briefly

Experimentation

RIXS experiments need high photon flux and are usually performed at synchrotrons. Table 3 shows an overview of RIXS experimental stations across the X-ray energy range. Two ranges are dominant: soft X-rays between 300 eV and 1,500 eV and hard X-rays above 4 keV. The extreme UV (XUV) range (30–300 eV) and tender X-ray range (1,500–4,000 eV) are used less often. The main X-ray edges are indicated in Fig. 4. Initial experiments are being performed at X-ray FEL sources and are included at the bottom of Table 3.

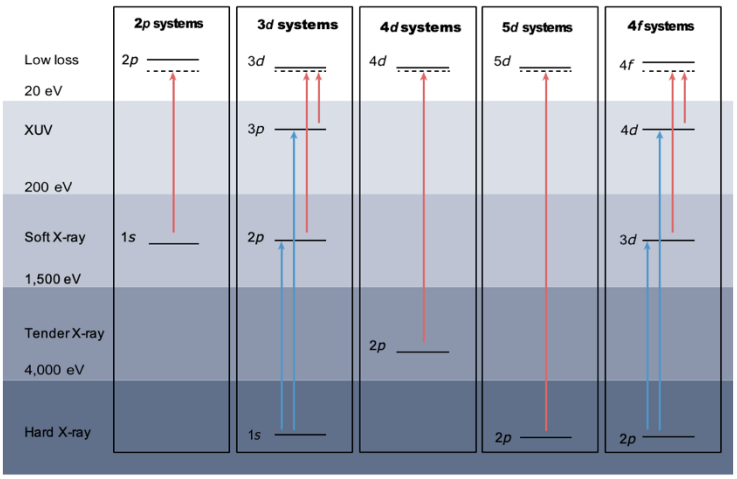

Fig. 4 | Overview of resonant inelastic X-ray scattering experiments on systems with an open 2*p*, 3*d*, 4*d*, 5*d* and 4*f* shell. The dashed line indicates low-loss features. Blue arrows indicate core resonant inelastic X-ray scattering (RIXS), for example, 1*s*2*p* (Kα) RIXS on 3*d* systems and red arrows indicate valence RIXS, in which the arrows indicate the movement of the (core) hole. The X-ray energy region is separated into extreme ultraviolet (XUV), soft X-rays, tender X-rays and hard X-rays, which correspond to the available beamlines and RIXS monochromators/detectors. The 1*s* core states range from the XUV range to the hard X-ray range, depending on the element. Not all possibilities have been indicated, for example, 4*f*5*d* RIXS might be interesting to study 5*d* systems.

Soft X-ray RIXS experiments

Soft X-ray RIXS (300–1,500 eV) beamlines and spectrometers typically use grating monochromators to analyse the X-ray beam delivered from the undulator source and scattered from the sample. The resolution of soft X-ray RIXS spectrometers has improved since the original designs[7]. Monochromators work at a grazing-incidence geometry. Consequently, a longer RIXS spectrometer will produce better energy resolution for a fixed combination of focal beam size, grating optics and detector. Over the past two decades, soft X-ray RIXS has flourished owing to markedly improved energy resolution, from 500 meV to 20 meV. To achieve this, the spectrometer length was increased from 1 m to 15 m and the surface quality of the grating optics was improved substantially with a better detector technology.

Table 3 | An overview of the resonant inelastic X-ray scattering beamlines at storage rings

Beamline	Synchrotron
XUV: 30–300 eV	
MERIXS[87]	Advanced Light Source (ALS), Berkeley, USA
UE112 (ref. 90)	BESSY, Berlin, Germany
SPECIES[254]	MAX-IV, Lund, Sweden
Soft X-ray: 300–1,500 eV	
ADRESS[7]	Swiss Light Source (SLS), Villingen, Switzerland
ID32 (ref. 8)	European Synchroton Radiation Facility (ESRF), Grenoble, France
I21 (ref. 9)	Diamond Light Source (DLS), Harwell, UK
SEXTANTS[255]	SOLEIL, Saclay, France
U41-PEAXIS	BESSY, Berlin, Germany
VERITAS	MAX-IV, Lund, Sweden
REIXS[256]	Canadian Light Source (CLS), Saskatoon, Canada
AMBER	ALS, Berkeley, USA
QERLIN	
Beamline 8.0.1	
SIX[10]	National Synchrotron Light Source (NSLS), Brookhaven, USA
41A[11]	Taiwan Photon Source (TPS), Hsinchu, Taiwan
BL11XU	SPRING8, Japan

BL07SU[257]	
IPÊ	Sirius, Brazil
Tender X-ray: 1,500–4,000 eV	
IRIXS[84]	Petra III, Hamburg, Germany
6-2a[258]	Stanford Synchrotron Radiation Lightsource (SSRL), Stanford, USA
ID26 (ref. 259)	ESRF, Grenoble, France
I21 (ref. 9)	DLS, Harwell, UK
Hard X-ray: 4,000+ eV	
ID26 (ref. 260)	ESRF, Grenoble, France
ID20 (ref. 13)	
BM30-FAME	
BM20-ROBL	
GALAXIES[261]	SOLEIL, Saclay, France
MARS	
I20	DLS, Harwell, UK
X-SPEC[262]	Karlsruhe Institute of Technology (KIT), Karlsruhe, Germany
SUPERXAS[263]	SLS, Villingen, Switzerland
BL12XU[264]	SPRING8, Japan
15-2 (ref. 265)	SSRL, Stanford, USA
20-ID[266]	Advanced Photon Source (APS), Argonne, USA
XFEL	
hRIXS	European XFEL, Hamburg, Germany
chemRIXS qRIXS	Linac Coherent Light Source (LCLS), Stanford, USA
FURKA	SwissFEL, Villingen, Switzerland

The list is divided into four energy ranges: extreme ultraviolet (XUV), soft X-rays, tender X-rays and hard X-rays. The fifth group of beamlines is located at X-ray free electron laser (XFEL) sources. The list is limited to beamlines that are dedicated to resonant inelastic X-ray scattering (RIXS).

Hard X-ray RIXS experiments

Hard X-ray RIXS (above 4,000 eV) is performed using perfect crystal Bragg optics. To obtain high energy resolution, each core resonance needs a crystal with backscattering conditions close to that energy. Two types of X-ray emission spectrometers are dominant: scanning and dispersive instruments. Scanning instruments use the available solid angle given by the crystal analyser surface at one emission energy in the spectrometer energy bandwidth. Dispersive instruments use the full spectrum across the surface of the position sensitive photon detector. Dispersive X-ray emission spectrometers have the advantage of simple, stable mechanics, whereas scanning instruments provide more flexibility with respect to the scan range. High-energy resolution fluorescence detection (HERFD) XAS is most efficiently carried out with scanning instruments as the entire available solid angle is used at the desired emission energy. Dispersive instruments enable single-shot XES measurements, which are particularly important for experiments at FELs. The optimal instrument geometry depends on the X-ray source, space constraints around the sample, required energy resolution and observed scattering process. Some instruments combine scanning geometry with a position sensitive detector to enable dispersion correction and improved energy resolution[83]. The analyser crystals must be of high quality to ensure good energy resolution.

Tender X-ray RIXS experiments

The tender X-ray range (1,500–4,000 eV) was historically less developed owing to slower monochromator development than in the soft X-ray and hard X-ray ranges. However, improved tender X-ray region resolu- tion has now been achieved. The IRIXS spectrometer at PETRA III uses a combination of multilayer mirrors and dispersing Ge(111) crystals to reach a resolution of 35 meV at the ruthenium L3 edge of 2,840 eV (ref. [84]). This enables many new experiments in the tender X-ray range[85]. Important areas in which tender X-ray RIXS experiments can provide insights are on sulfur, phosphorous and 4d transition metal systems.

XUV RIXS experiments

XUV RIXS experiments with energies between 30 eV and 300 eV are not often studied. This is due to low signal and large elastic peaks from scattering, which make it challenging to study low-energy excitations. As an example, XUV RIXS experiments at the copper 3p XAS resonance on Sr2CuO2Cl2 samples were performed on beamline 7 at the Advanced Light Source[86], where the MERIXS end station was built to measure XUV RIXS[87]. This set-up has been used to study 3p valence RIXS on cobalt, nickel and copper systems[88]. At the SIS beamline at the Swiss Light Source, 3p valence RIXS spectra of NiO were measured[89]. A new end station at BESSY[90] has a lower incident energy, potentially improving the overall energy resolution.

Sample conditions and X-ray-induced effects

Hard X-ray RIXS has an attenuation length from 5 µm to 20 µm, enabling experiments under a wider range of conditions in transition metal oxides. Catalysis experiments are possible under operando conditions using chemical reactors and high-pressure cells. Tender X-rays have attenuation lengths of 0.5–2 µm, which also allow experi- ments to be performed under operando conditions but requiring more dedicated reactor cells. Soft X-ray RIXS has attenuation lengths of 100–300 nm, needing more complex dedicated reactor designs. The high vacuum design of soft X-ray RIXS end stations limits the use of gases and liquids, which could potentially damage optical components. Most high-resolution soft X-ray RIXS beamlines operate under vacuum. However, there are dedicated soft X-ray RIXS beamlines for operando conditions at lower resolution, for example, BL07SU at SPRING8 and VERITAS at MAXIV. These instruments are tailored to RIXS studies of applied physics, energy materials and catalysts. XUV RIXS experiments have attenuation lengths below 100 nm and can only be performed in vacuum. As a photon-in–photon-out technique, RIXS experiments can be performed with an applied electric or magnetic field. For solid-state samples in most of RIXS experiments, the relatively large penetration depth means that sample preparation is straightforward, without need- ing special care. However, if looking at low-energy collective excita- tions, single-crystal samples are required with post-cleaving to give a flat surface that minimizes the elastic scattering signal. Sample align- ment before experiments is useful to project low-energy excitations in a specific direction in the momentum space. These valence RIXS experiments need a very high-energy-resolution set-up in soft X-ray, tender X-ray and hard X-ray energy range for 3d, 4d and 5d transition metal oxides, respectively.

RIXS experiments need a high-intensity X-ray beam, which can result in X-ray-induced effects or damage. This is especially important for soft X-rays owing to lower attenuation length and non-radiative decay channels. Core holes in the soft X-ray range decay more than 90% by Auger decay, yielding lower RIXS efficiency and a greater chance of X-ray-induced damage. Core holes in the hard X-ray range decay less than 50% via Auger decay. X-ray-sensitive experiments are more likely to be measured by X-ray absorption than RIXS because XAS requires a lower X-ray intensity. To reduce or avoid damage, fresh samples can be used at a high repetition rate. In liquid jet experiments, every X-ray pulse probes a fresh sample if the jet speed is sufficiently high and/or the time between X-ray pulses sufficiently large. This means that potential damage effects will only occur at the synchrotron X-ray pulse length of ~100 ps or the XFEL pulse length of a few tens of fs. Solid samples sensitive to the X-ray beam can be raster-scanned. The raster speed is optimized to the measured damage effects, but the sample must be homogeneous over the scanned region and detected sample volume.

Results

This section divides RIXS experiments into core and valence RIXS. In valence RIXS, the core hole created in the first step (X-ray absorption) is filled by a valence electron. In core RIXS, a deep core level in the intermediate state is replaced by a shallow core level in the final state.

Valence RIXS

In valence RIXS, the system is left with an excitation that does not involve a core hole. Valence excitations include vibrational, magnetic and electronic excitations. Molecular systems show vibrational struc- ture, and isolated transition metal ions have low-energy (<500 meV) excitations owing to spin–orbit coupling and small

symmetry distor- tions. In solids, low-energy (<500 meV) collective excitations have been widely observed, including phonons and magnons from strong electron–phonon and spin–orbit coupling, respectively. Exploring low-energy collective excitations is important in studies of quantum materials based on 3d, 4d and 5d transition metal elements. For 3d transition metals, kinematic constraints between the soft X-ray energy and wave vector means that the maximum momentum transfer is smaller than a Brillouin zone. The accessible range is much larger for 4d and 5d transition metals owing to the higher X-ray energy. The momentum transfer in RIXS can be expressed as:

$$Q(\text{Å}^{-1}) = \frac{4\pi}{\lambda} \sin\frac{\theta}{2} \sin\left(\varphi - \frac{\theta}{2}\right)$$

in which λ is the wavelength of the incident X-ray; ϕ is the grazing- incident angle between the incoming X-ray and sample surface and θ is the scattering angle between the incoming and outgoing X-rays. At the copper L3 edge, the maximum momentum transfer (at θ = 150°) is 0.85 Å−1, which is not enough to cover the first Brillouin zone.

Above 500 meV, electronic excitations from electron–hole pairs are found. For example, in 3d systems, dd excitations (<5 eV) are related to different configurations of the 3dN manifold. For an isolated 3d ion in a molecule or a solid, dd excitations are fixed at a specific energy. This enables accurate determination of the crystal-field splitting and electron–electron interactions5 similar to optical spectroscopy. The advantage of RIXS is its element selectivity, which can isolate metal-centred excitations and distinguish the behaviour of different metal ions in systems with multiple metal ions. In solid systems, the dd excitations, or orbitons, are momentum-dependent. Above 3 eV, the observed charge-transfer excitations are related to transitions from 3dN to 3dN+1L, in which the charge-transfer notation 3dN+1L refers to the excitation of an electron from a ligand valence band state to the 3d state.

Valence RIXS at the K edge of 3d transition metals may either involve dipole excitations to the main edge or quadrupole and dipole transitions to the pre-edge. Resonant excitations to the main edge have been used to study collective excitations91. However, the absence of spin–orbit interaction in the 1s core hole limits the type of excitations that can be observed. Valence RIXS at the main edge of a copper-oxide system has been studied. When the system is excited above the edge resonance, charge-transfer excitations are visible in the final state with polarization and momentum dependence92. This RIXS process is referred to as indirect RIXS. This has been studied, for example, in La_2CuO_4 (ref. 92) and Nd_2CuO_4 (ref. 93). Charge-transfer excitations in indirect RIXS are different from those visible at the XAS edge, referred to as direct RIXS in this context (see Supplementary information for more details).

Core RIXS

In core RIXS, a deep core level in the intermediate state is replaced by a shallow core level in the final state. For example, a 2p electron decays to a 1s core hole in 1s2p RIXS. A core hole potential acts on valence electrons in the intermediate and final states, even though its magnitude will vary slightly94. Consequently, charge-transfer excitations that are present and shifted in energy in the intermediate state will also be present and shifted in energy in the final state. In valence RIXS, there is no core hole potential in the final states and excitations separated by the core hole potential in the intermediate state appear at similar final state energies. As a result, comparing core and valence RIXS can help identify the nature of the excited states and probe theoretical models94,95.

The RIXS plane of band excitations can be approximated as a convolution between the XAS and XES spectral shapes. For instance, 1s2p RIXS relates to 1s XAS and 1s2p XES. It is recommended to check whether the measured RIXS plane can be simulated from the XAS and XES components. This is not easily observed in the RIXS plane directly because the combination of a structured XAS and XES spectrum can produce complex variations in the RIXS plane. Comparing the RIXS plane and XAS–XES convolution is also important because any features that cannot be reproduced can be used to pinpoint exciton-induced peaks96.

1s2p RIXS in 3d transition metals combines K pre-edge and L edge absorption spectroscopy, whereas the hard X-ray probe ensures bulk sensitivity and compatibility with in situ conditions. Figure 5a shows an example of a full 1s2p RIXS plane, in which it is challenging to extract all information owing to dipole and quadrupole transitions in the pre-edge from pd mixing. In the K pre-edge, there are multiple excitonic states. For octahedral symmetry, the K pre-edge can be approximated as a 1s3d quadrupole transition. The 1s2p RIXS spectrum can then be calculated as 3dN > 1s13dN+1 > 2p53dN+1. The final states are identical to those in 2p XAS (3dN > 2p53dN+1), but the spectrum is different owing to different XAS and XES matrix elements97. Similarly, 1s3p RIXS reaches the same final state as 3p XAS. In the 1s2p RIXS plane of CoO, the pre-edge RIXS structure can be reproduced from 3d7 > 1s13d8 > 2p53d8 calculations98. The 2p3s core RIXS of CaF_2 has been measured99,100 and could be explained by multiplet calculations of the 3d0 > 2p53d1 > 3s13d1 transitions101. This 2p3s XES channel is important for partial fluorescence yield measurements because it does not suffer from the distortions that are present in the dominant 2p3d valence RIXS channel102.

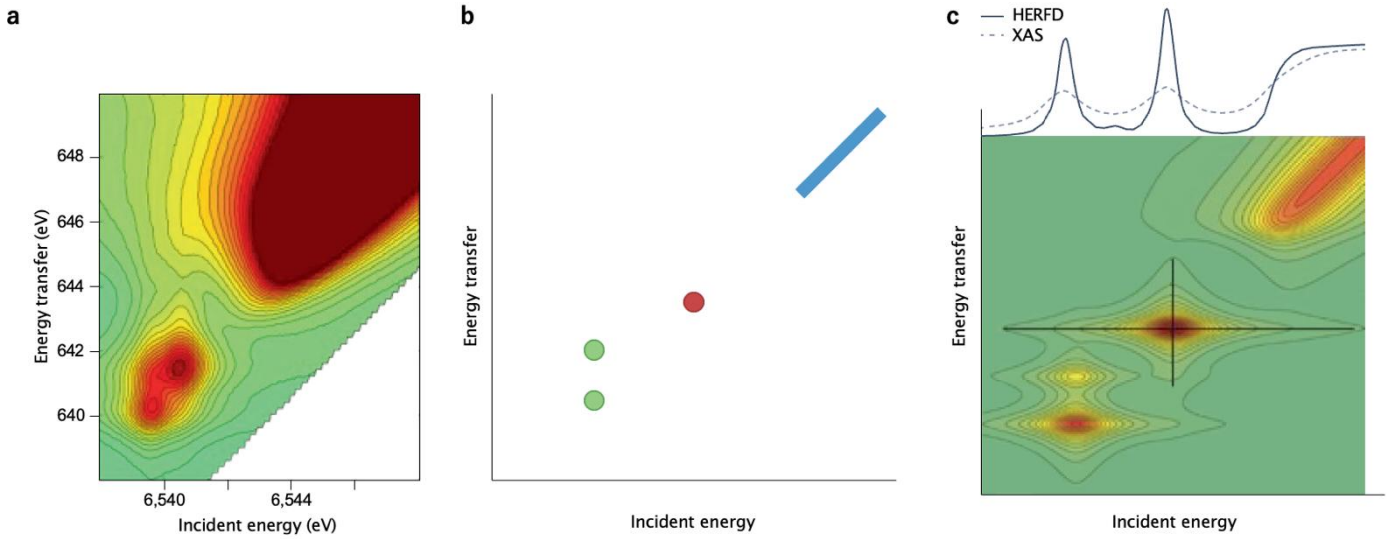

Fig. 5 | Overview of the 1*s*2*p* resonant inelastic X-ray scattering map. a, Contour plots of manganese 1*s*2*p* (Ka_1) resonant inelastic X-ray scattering (RIXS) planes of MnO. **b**, An excitation into a broad band becomes a diagonal streak (blue) in the RIXS plane. **c**, Including the spectral broadenings arising from the core hole lifetimes gives the intensity distribution in the RIXS plane. The line scans compare an X-ray absorption spectrum (XAS) with a high-energy resolution fluorescence detection (HERFD) XAS spectrum that is recorded along a diagonal line through the RIXS plane. Panel **a** adapted with permission from ref. 267, American Chemical Society.

High-energy resolution fluorescence detection

The spectral broadening arising from the short lifetime of a deep core state can be removed103, although it will still affect the spectral shape. This was first achieved using the 2p3d RIXS channel when scanning through the 2p XAS L3 edge spectrum of dysprosium. By recording the dysprosium 2p3d (Lα1) line with an instrumental bandwidth below the 2p core hole lifetime broadening, spectral broadening was reduced. This experimental technique was later termed HERFD XAS. For isolated, sharp resonances, 2p lifetime broadening is replaced by the 3d lifetime broadening, in which multiplet effects in excitonic states do not allow the spectra to be interpreted as measurements of the X-ray absorption coefficient104. HERFD XAS has been used at the K edge of 3d transition metals recording the Kα (1s2p) or Kβ (1s3p) lines and at the L edge of 5d transition metals using the Lα line (2p3d). Figure 5 shows that in a multipeaked exciton spectrum, the HERFD spectrum is modified with respect to the original XAS spectrum77,105. HERFD XAS at the L edges of 4d and 5d transition metals provides a good approximation of the line-sharpened absorption cross-section. Similar results were found at the M and L edges of actinides106,107. Pre-edges observed at rare-earth L edges and 3d transition metal K edges can show strong multiplet structures that require more careful theoretical analysis. Exciting several electronvolts before an X-ray absorp- tion edge results in observation of an approximately inverted XAS spectral shape, known as the high-energy-resolution off-resonance spectroscopy108, which has the advantage of being insensitive to self-absorption effects.

Selective X-ray absorption

Core RIXS spectra can be used for selective XAS experiments. In a system with a metal in two valence states, the chemical shift in the XES spectra can disentangle the XAS spectra of the individual valences. This has been used for the mixed Fe2+/Fe3+ system Prussian blue to derive valence-selective XAS spectra[109]. Another option is to use the 1s3p XES channel to split the XAS spectrum into spectra that favour spin-up or spin-down components. This procedure can measure spin-polarized XAS spectra[110,111], for instance, identifying high spin Fe(IV) as the 3d4 configuration enables spin up excitations that are forbidden in a high spin Fe(III) system. Several systems in (bio)catalysis are proposed to involve high spin Fe(IV) in the catalytic cycle and could benefit from this spectroscopic technique[112].

Angular-dependent and polarization-dependent RIXS

By measuring the polarization of the incident and/or emitted X-rays, angular, polarization and scattering geometry-dependent RIXS can be performed. Calculations before the experiment can find the best experimental configuration to identify the origin of excitations. Polarization-dependent RIXS measurements have mainly been performed on ferromagnetic/ferrimagnetic materials with broken time- reversal symmetry in RIXS-MCD. RIXS-MCD has even investigated weak ferromagnetism, such as in α-Fe2O3, which is not possible with X-ray MCD[113–115]. The nature of the excitation can be discriminated with RIXS-MCD, for example, by differentiating between spin and charge excitation in cuprates[54,116]. For 3d transition metals[117], hard X-ray RIXS- MCD is a valuable alternative to soft X-ray MCD when in situ conditions in dedicated sample environments are required — such as colloidal mag- netic nanoparticles[118,119] — and for materials in which the surface is not representative of bulk properties, such as buried magnetic layers[117] and core–shell nanoparticles. The angular dependence of iron 2p3d RIXS has been used to study the origin of the metal-to-insulator transition in Fe3O4 (ref. [120]). RIXS-magnetic linear dichroism revealed that the lowest-energy state of the high-temperature phase of Fe3O4 arises from an intri- cate interplay among crystal-field, exchange and spin–orbit interactions. This suggests that trimerons, three-site polarons, in the low-temperature phase are not identical to trimerons in the high-temperature phase[121].

At soft X-ray RIXS beamlines, outgoing beam polarization analysis was first performed using a graded multilayer to disentangle σ-polarized and π-polarized components in the scattered beam[12]. This showed the collective nature of spin excitations in cuprates[35,122,123]. At hard X-ray RIXS beamlines, a polarization detector is based on a diamond phase retarder. This was used to measure an MCD effect in the iron 1s2p (Kα1) X-ray emission in an α-iron single crystal[124]. Polarization analysis substantially reduces the number of detected photons; however, extreme brilliant sources and XFELs could lead to future developments.

Magnetic excitations

RIXS can be used to measure magnetic excitations[24,51,57], making it comparable to INS[125]. For INS, the operator that generates spin excitations is $F(q)S\perp q$, in which F(q) is the element and environment-dependent atomic form factor and $\mathbf{S}\perp\mathbf{q}$ is the spin operator perpendicular to the transferred momentum $\mathbf{q}$. For RIXS, the effective operator that generates single spin excitations at site j is $\sigma^{(1)}_j(\omega)\boldsymbol{\varepsilon} \times \boldsymbol{\varepsilon}\cdot\mathbf{S}$ for light with incoming energy $\hbar\omega$, polarization ε_i and scattered polarization ε_o [24] (Supplementary information). This has enabled measurement of sin- gle magnon excitations in cuprates, nickelates and iridates, discussed in the Applications section[25,26].

Multimagnon excitations from modification of the intermediate- state exchange interaction can also be obtained[24,51]. Here, the excitation operator has the form $J_{i,j}\,\mathbf{S_i}\cdot\mathbf{S_j}$, with i and j relating to neighbouring lattice sites and J a polarization-dependent and resonant-energy-dependent atomic form factor. This operator means that there can be $\Delta Sz = 0$ multimagnon excitations. This is the leading mechanism to excite magnetic excitations, particularly at the K edge with an s core hole without active spin–orbit coupling[24]. By contrast, at transition metal L edge, owing to the large 2p spin–orbit coupling and 2p3d exchange interaction, multiple spin-flip excitations could occur on the same magnetic site. In NiO, the antiferromagnet with 3d8 Ni^{2+} (S = 1)

ions, besides the single magnetic excitation, there is an additional excitation in which two spin-flip excitations occur on the same nickel site[42].

Applications

Copper-oxide superconductors

Copper-oxide superconductors (cuprates) are an important quantum material owing to their intriguing low-energy physics and the super-conductivity with critical temperature Tc as high as 165 K. It is generally accepted that the intrinsic nature of cuprates is from the CuO2 square planar structure, characterized by a strong electronic correlation and antiferromagnetic superexchange interaction. In the past two decades, copper L edge valence RIXS has made a large contribution to the study of cuprates. With improved energy resolution below 1 eV, copper L edge RIXS is a useful tool for systematic studies of dd orbital and charge-transfer excitations in cuprate oxides[126,127]. Owing to the high-energy resolution (~100 meV) and ability to probe the momentum space, RIXS is capable of investigating elementary magnetic excitations — magnons or two-spinons — in bulk single crystals and thin films[51,128,129]. Many RIXS experiments have studied magnons and paramagnons, whose doping- dependent behaviour helped understand the spin degree of freedom in cuprates and relationship to the superconducting pairing mechanism[21,125,129–131]. High-resolution RIXS mapping of magnons in the detailed energy and momentum spaces revealed the interplay among the super-exchange interaction, crystal structure and superconducting transition temperatures[132,133]. Besides the copper L edge, RIXS at the oxygen K edge can provide valuable information about magnetic excitations, such as bimagnons and four-spinons[134–136]. The polarization analysis of the outgoing X-ray enabled copper L edge RIXS to reveal the spin character of multimagnons in the specific momentum space in cuprates[45,137].

Charge carriers alter the parental insulating phase to an unusual metallic phase and exotic ordering states — such as spin or charge density modulations — often form below and are thought to be relevant in high-temperature superconductivity. Over the past decade, the extreme sensitivity of valence RIXS to the scattering signal has led it to play a critical role in the study of weak short-range ordered CDWs and their fluctuations in cuprate superconductors[138–141]. High-energy resolution valence RIXS showed that CDW excitations have a characteristic funnel shape that interferes with electron–phonon excitations[34,142,143]. Figure 6a shows a typical CDW scattering peak located at ~0.25 relative lattice units in a single-layered bismuth-based cuprate superconductor, $Bi_2Sr_{1.4}La_{0.6}CuO_{6+\delta}$, the RIXS phonons (~70 meV) and the interference between them[143]. With improved experimental efficiency, excitonic excitations were discovered in cuprates and are thought to have an intimate relationship with the pseudogap state[144]. Collective 3D acoustic plasmons were theoretically predicted to exist in cuprates decades ago. They were eventually experimentally confirmed by high-resolution RIXS in both electron-doped and hole-doped cuprate superconductors[145–148]. The ability to probe the energy–momentum space via various elements adds extra value for in-depth understanding of plasmon physics[149,150]. Figure 6b,c displays RIXS results at the oxygen K edge on two independent cuprate superconductors: $La_{1.84}Sr_{0.16}CuO_4$ (LSCO) and $Bi_2Sr_{1.6}La_{0.4}CuO_{6+\delta}$ (Bi2201). Remarkably, the acoustic plasmons show unambiguously the dispersion along the c-axis having a minima at $l = 2\pi/c$, in which c is the lattice constant along the out-of-plane direction but different for each cuprate system[146].

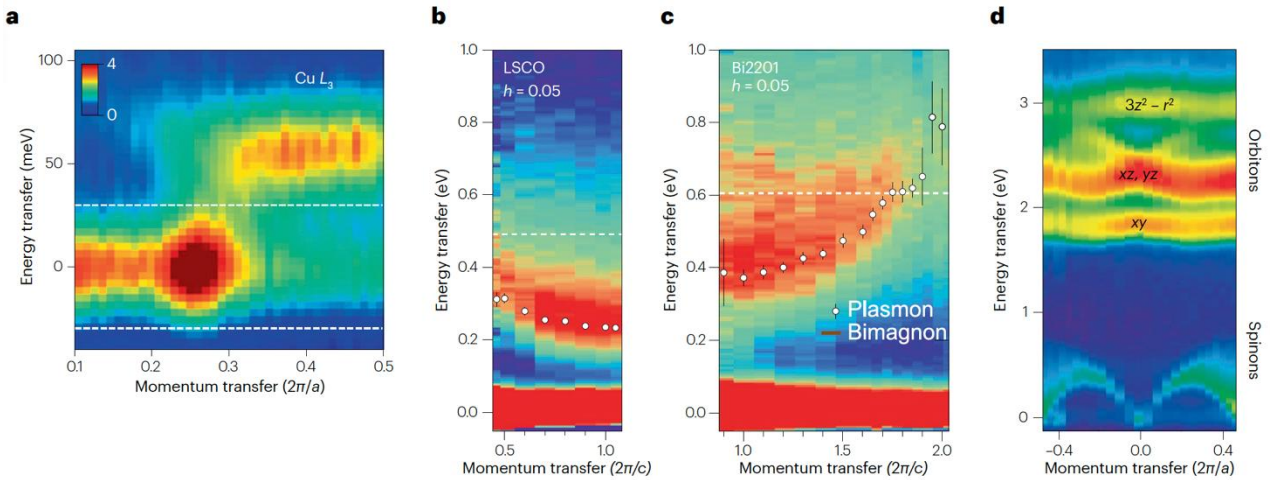

Fig. 6 | Momentum dependence in cuprates. a, Charge density waves observed at the copper L_3 edge in $Bi_2Sr_{2-x}La_xCuO_{6+\delta}$. **b**,**c**, Acoustic-like plasmon excitations in $La_{1.84}Sr_{0.16}CuO_4$ (LSCO) (panel **b**) and $Bi_2Sr_{1.6}La_{0.4}CuO_{6+\delta}$ (Bi2201) (panel **c**) superconductors probed by resonant inelastic X-ray scattering. **d**, Spin–orbital separation in 1D Sr_2CuO_3. The low-energy excitations are dominated by two- spinon continuum. The higher-energy part contains the dispersive orbitons. Panel **a** adapted from ref. 143, CC BY 4.0. Panels **b** and **c** adapted from ref. 146, CC BY 4.0. Panel **d** adapted from ref. 26, Springer Nature Limited.

Magnons are collective excitations arising from a spontaneously broken magnetically ordered state. Likewise, the collective orbital excitations, orbitons, may exist in a spontaneously broken orbitally ordered state. Exploration of orbitons is ongoing in colossal magnetoresistant manganites owing to the importance of the orbital degree of freedom[151]. One-dimensional cuprate spin chains are marked by quantum fractionalization, the breaking-up of the elementary electron into its separate degrees of freedom, such as spinon and holon[152]. The same principle should hold to the orbital degree of freedom. RIXS experiments showed that an orbiton separating itself from two-spinons propagates through the lattice as a distinct quasiparticle with a substantial dispersion in energy andmomentum space[26] (Fig. 6d). In a recent high-resolution RIXS study, orbitons were found in 2D cuprates without apical oxygens[153]. The dispersion is ascribed to a substantial next-nearest neighbour orbital superexchange within the CuO_2 planes.

Iron-based superconductors

Iron pnictides and chalcogenides (FeSC) with tetrahedrally coordinated ligands from group V and group VI are known to host unconventional superconductivity with a critical temperature Tc above 100 K in FeSe thin films154. Although angle-resolved photoemission spectroscopy and INS have made notable contributions to the understanding of the electronic band structure and magnetic excitations in FeSC, RIXS has also had a critical role in unravelling the magnetic excitations, especially at the high-energy range. Most FeSC compounds are metallic, showing itinerant character in both charge and orbital degrees of freedom. An early soft X-ray iron L edge RIXS study on FeSC revealed weak Coulombic correlation, iron metallicity and strong covalency in these materials155. Such itinerant electronic state is manifested by the dominating iron 3d X-ray fluorescence emission in most FeSC compounds. The majority of FeSC compounds order magnetically, with a stripe pattern below a critical temperature, whereas some — such as FeSe — show short-range magnetic fluctuations. An early high-resolution RIXS study showed that the optimally hole-doped superconducting $Ba_{0.6}K_{0.4}Fe_2As_2$ retains well- defined and dispersive high-energy magnetic excitations compared with the magnons of undoped antiferromagnetic $BaFe_2As_2$ (ref. 23).

The persistence of magnetic excitations well into the superconduct- ing phase suggests the robustness of local fluctuating moments in FeSC superconductors. High-energy magnetic excitations were also found in cobalt-doped NaFeAs, although the bandwidth has less dop- ing dependence156. Iron Kβ-RIXS on hole-doped and electron-doped $BaFe_2As_2$ revealed that the local magnetic moment is nearly constant in hole-doped samples but decreases on electron doping157. Most FeSC superconductors manifest a tetragonal-to-orthorhombic transition, known as electronic nematic order, whose physical origin is still under debate. By applying high-resolution RIXS in a mechanically detwinned FeSe bulk single crystal, it was found that high-energy magnetic excitations (~200 meV) manifest a strong anisotropy, disappearing around the nematic transition

temperature158. As the large magnetic energy scale exceeds the orbital splitting energy, RIXS results sug- gest that the nematicity in FeSe is likely spin-driven. High-resolution RIXS probed a monolayer of FeSe, in which the magnetic excitations were found to be distinct from the bulk crystal159. The ability to probe the FeSe monolayer demonstrates that high-resolution RIXS is a powerful tool for studying small thin films, exfoliated 2D materials and operando microdevices.

Nickelates

Nickelates are a large family of quantum materials with fascinat- ing physical properties. $RNiO_3$ (R = rare earth) is characterized by a metal–insulator transition and complex electronic and magnetic structures160. Striped charge and spin ordering are present in hole- doped $R_{2-x}Sr_xNiO_4$ that have been extensively studied by X-ray and neutron scattering161,162. In 2019, superconducting $Nd_{0.8}Sr_{0.2}NiO_2$ thin films that are isostructural to infinite-layer cuprates were successfully synthesized, leading to the demonstration of superconductivity in many other rare-earth infinite-layer nickelates and quintuple-layer $Nd_6Ni_5O_{12}$ (refs. 163,164). Under a moderately high pressure, the bilayer nickelate $La_3Ni_2O_7$ is driven to the superconducting state at a critical temperature of ~80 K (ref. 165). After RIXS was found to be a probe of collective magnons in cuprates, collective magnons were revealed in R2−xSrxNiO4, consistent with INS166. Detailed energy-dependent RIXS work on NdNiO3 discovered predominant 3d8 orbital character in support of negative charge transfer and bond disproportionation167. Using the site selectivity of RIXS in $NdNiO_3$, rich collective magnetic excitations from disproportionated NiO_6 octahedra were discovered in agreement with the complex spin interaction168. High-resolution RIXS has contributed to the study of infinite-layer nickelate super- conductors. By combining XAS and RIXS at both nickel L and oxygen K edges in $RNiO_2$, sizable hybridization between rare-earth 5d and nickel 3d orbitals was revealed. In addition, the Ni3d-O2p orbital hybridization was found to be much weaker than NiO and perovskite $RNiO_3$, suggesting that infinite-layer nickelates are closer to the Mott–Hubbard than the charge-transfer regime169. Despite the absence of long-range antiferromagnetic ordering, well-defined and strongly dispersive magnons in $R_{1-x}Sr_xNiO_2$ were characterized by high-resolution RIXS, demonstrating strong electronic correlation and superexchange interactions, comparable to cuprates170,171. A similar nearest-neighbour superexchange interaction was revealed by RIXS in the trilayer low-valence nickelate $R_4Ni_3O_8$ (ref. 172). Concerning the low-energy physics of $R_4Ni_3O_8$, oxygen K edge RIXS shows that a considerable amount of the oxygen 2p states has a mixed charge-transfer Mott–Hubbard character173. Similar to $R_{2-x}Sr_xNiO_4$, stripe-phase charge ordering is developed in R4Ni3O8 and RIXS could accurately determine the orbital character of the state with multiplet theory174. A translational-symmetry-breaking state was reported by RIXS in various infinite-layer nickelates, despite debatable origin175–178. As shown by recent RIXS work on La3Ni2O7, multiple orbitals are involved in the low-energy physics, including nickel 3dx2−y2, nickel 3dz2 and ligand oxygen 2p orbitals with a small charge-transfer energy (~0.5 eV). In addition, the RIXS polarization analysis identified the dispersive mode and ordering state as being of spin origin179.

High-order magnetic excitations

Using high-resolution RIXS, single-site multimagnon excitations are observed in α-Fe_2O_3 (refs. 43,44). The ground state of Fe^{3+} in α-Fe_2O_3 is $^6A_1$, with S = 5/2. In principle, this allows the local spin to be changed five times. Experiments show one, two, three and four magnon peaks. The one and two magnon transitions can be explained from core hole spin– orbit splitting, whereas the three and four magnon need an additional effect from the crystal lattice to conserve the spin degrees of freedom. The five magnon peak is likely too small to distinguish from the experi- mental background. Multimagnon excitations can be understood as a convolution of several non-interacting single magnon excitations, in which the sum of the momentum of all excited magnons corresponds to the transferred momentum. If interactions between magnons are present, additional multimagnon bound states can form. This has been observed in a 1D spin-chain compound Y_2BaNiO_5 (S = 1)180 (Fig. 7a–d). Local ΔSz = 2 excitations are also known as quadrupolar spin excitations and the ΔSz = 1 as dipolar excitations. This nomenclature is related to the Stevens expansion of the transition operator in multipoles of the spin operator S. It is found that the quadrupolar magnon can propagate as a

bound quadrupolar magnetic wave, or two independent triplets, elucidating a rich phase of higher-order magnetic excitations[180]. By probing both the bound magnon states and the continuum of two free magnon excitations, in principle, the full momentum-dependent magnon interactions can be studied.

Magnetic topology and itinerant magnetism

Magnetic topological materials are a class of compounds with prop- erties determined by the topology of the low-energy electronic band structure and the spin configuration[181]. Among them, topological Kagome magnets are the birthplace of emergent phenomena owing to the interplay among geometry, topology, spin and electronic correlation[182]. In the Kagome lattice, the destructive quantum phase interference of electron hopping pathways enhances the electronic interaction and often a flat electronic band is formed in momentum space. The combination of correlated flat bands and topological states has led to many exotic phenomena, including fractional Chern physics, CDWs, ferromagnetism and unconventional superconductivity[182]. To advance the understanding of band topology-driven magnetism, it is crucial to study the flat band magnetic excitations in these materials. A recent high-resolution RIXS study discovered a well-defined and near flat-band-like Stoner excitation in a Kagome Weyl semimetal $Co_3Sn_2S_2$. Figure 7e–h shows that the nearly non-dispersive Stoner spin excitation peaks are formed in sharp contrast to the featureless Stoner continuum in conventional itinerant ferromagnet metals[183]. This observation opens a pathway for further studies of band-induced symmetry-breaking orders in topological materials.

Using soft X-ray valence RIXS, magnons were also observed in ferromagnetic iron and nickel metals. The magnons disperse as expected near the Brillouin zone centre and are damped at higher q values owing to interaction with particle-hole Stoner excitations[184]. This damping usually results in a reduced magnon lifetime. A recent RIXS study found that the metallic antiferromagnet $CeCo_2P_2$ exhibits long-lived magnons even in the terahertz regime owing to the suppression of Stoner excitations[185]. Spin excitations are typically studied by INS in bulk materials; however, the large penetration depth of neutrons means that the behaviour in mesoscopic films is elusive for INS. Soft X-ray valence RIXS is, therefore, ideally suited toexploring spin excitations in confined thin films. An iron thin film was found to have ferromagnetic spin excitations that renormalize to lower energies in the out-of-plane direction owing to the confinement effect, while retaining dispersion in the in-plane direction[186].

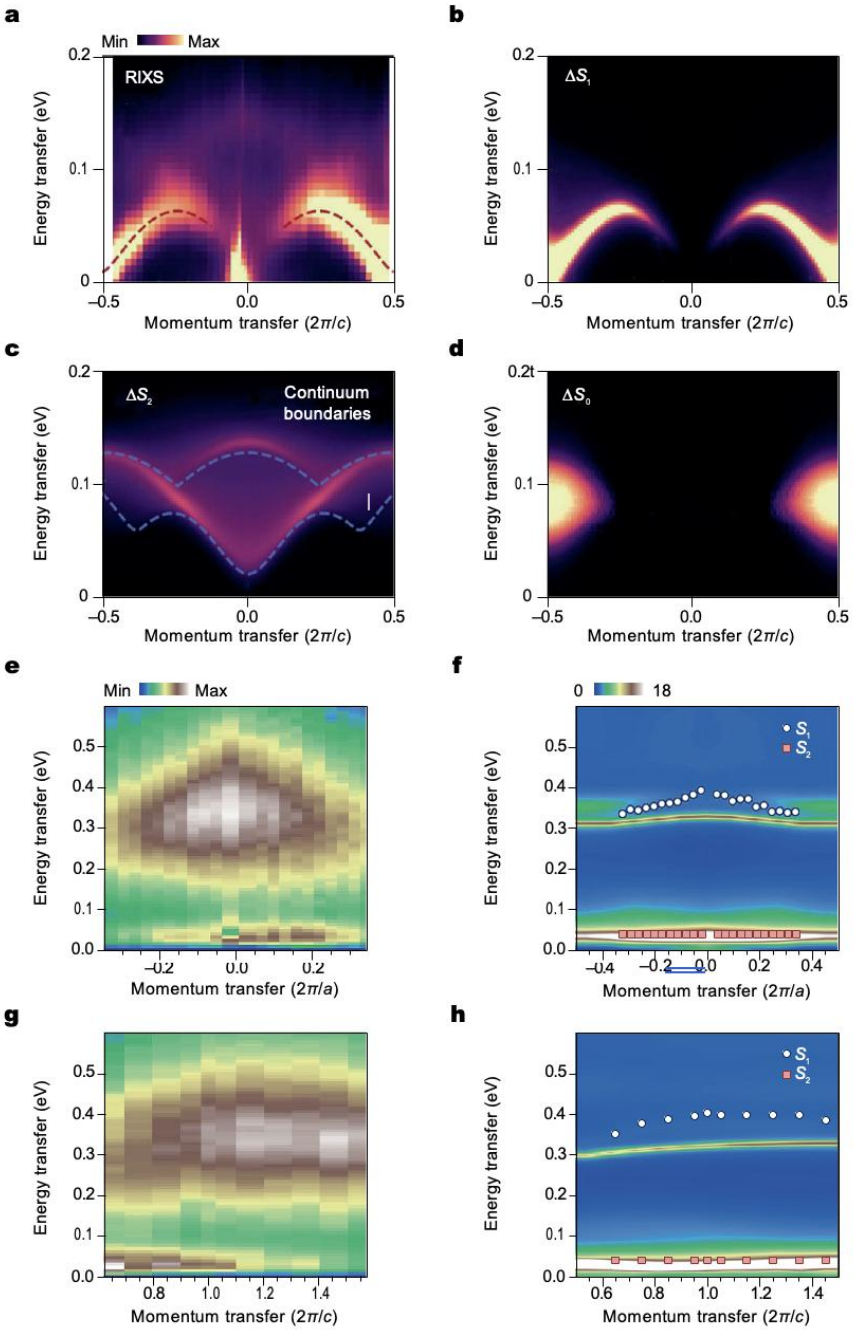

Fig. 7 | Magnetism applications. **a**, Magnetic excitations observed in 1D spin-chain Y_2BaNiO_5 (ref. 180). **b**, Density matrix renormalization group (DMRG) calculations of the dipolar magnon. **c**, DMRG calculation of the quadrupolar magnon. **d**, DMRG calculation of two-site spin-conserved excitations ($\Delta S = 0$). **e**,**g**, Near flat-band Stoner excitations observed in $Co_3Sn_2S_2$ along the *h* direction (panel **e**) and *l* direction (panel **g**) (ref. 183). **f**,**h**, Comparison of the flat-band Stoner excitations with the dynamical spin susceptibility computed by the dynamical mean-field theory. RIXS, resonant inelastic X-ray scattering. Panels **a–d** adapted from ref. 180, Springer Nature Limited. Panels **e–h** adapted from ref. 183, Springer Nature Limited.

4d materials including ruthenates

Compared with 3d transition metal systems, 4d systems have increased 4d spin–orbit coupling and larger crystal field, combined with larger covalence and smaller local correlations. Valence RIXS in 4d transition metals is studied in the soft X-ray range at the oxygen K edge and the ruthenium 3p (M2,3) edge. Tender X-rays are used at the ruthenium 2p (L2,3) edge, in which a larger momentum range can be achieved. Polarization- dependent oxygen K edge RIXS reveals the spin and orbital excitations, providingnew details aboutthe interplay ofcrystal-field and spin–orbit effects in Ca2RuO4 (ref. 40) and Ca3Ru2O7 (ref. 187). The combination of oxygen K edge and ruthenium M3 edge RIXS can disentangle the contributions of crystal-field, spin–orbit and local correlations in $RuCl_3$ (ref. 188) and RuO2 (ref. 189). Ruthenium 2p RIXS was also used to study these excitations in $RuCl_3$, in which distortions of the RuCl6 octahedra were observed near the

surface190. The momentum dependence of magnetic excitations has been studied with ruthenium 2p RIXS for the SrRu2O6 (ref. 191) and K2RuCl6 system192. Magnons and dd excitations have been observed in MoO3 (ref. 193). HERFD and core-to-valence RIXS measurements have been performed on a series of ruthenium coordination complexes194.

5d materials including iridates

Compared with 4d transition metal systems, 5d systems have an increased 5d spin–orbit coupling but similar crystal field and local correlations. Valence RIXS of the L3 edge of 5d transition metals is in the hard X-ray range in which iridates, rhenates and osmates are studied. Using instruments with energy bandwidth of ~20 meV, it is possible to study collective excitations and address fundamental questions about the importance of spin–orbit interactions in the 5d shell. The combined effect of the crystal field, local correlations, exchange and 5d spin–orbit coupling has been studied in the spin–orbit Mott insulators Sr_2IrO_4 (refs. 22,195,196) and Li_2IrO_3 (ref. 197). Similar results were found for $Sr_3Ir_2O_7$ (ref. 198) and Ba2YReO6 (ref. 199). The theoretical description of iridates found a dispersion of excitations with different symmetries200. L edge RIXS was used in an atomic-scale Young double-slit experiment using iridium dimers in $Ba_3CeIr_2O_9$ as slits, in which the interference patterns prove the coherence of the scattering process201. Using the oxygen K edge RIXS in Sr_2IrO_4 and $Sr_3Ir_2O_7$, collective single and bimagnons, spin–orbit and electron–hole excitons were observed owing to strong spin–orbit coupling in the ground state196,202. Oxygen K-RIXS was also used to compare the momentum-resolved spin–orbit excitons in Ba2IrO4 (ref. 203) and Sr2RhO4 (ref. 204).

Rare-earth 4f systems

RIXS spectra of rare-earth systems have been systematically calculated based on the atomic multiplet theory205,206. The 4d4f RIXS spec- tra of DyF_3 were measured through the 4d XAS, and the 4d4f RIXS spectra were calculated using the multiplet theory, in which they are sensitive to crystal-field effects207. Although the crystal field is only 35 meV, it can be detected with 100 meV resolution as it creates new peaks owing to modified selection rules. A 3d4f RIXS study on CeO_2 revealed the presence of charge-transfer states and the charge-transfer multiplet analysis showed that with 4f0 and 4f1 configurations, hopping between configurations is lowered in the intermediate core hole state49. Recent improvements in energy resolution have enabled more detailed RIXS studies of 4f systems. The crystal-field splitting of the 6H5/2 ground state of Sm3+ in the strongly correlated topological insulator SmB6 was determined with 3d4f RIXS, enabling separate determination of crystal-field-split excited multiplets of Sm3+ and Sm2+ ions208. With 3d4f RIXS, it was found that the cerium 4f crystal-field strength is too small to explain the strong reduction of the cerium magnetic moment in CeRh3B2. Instead, there are two different active cerium 4f orbitals209.

Actinide 5f systems

A range of RIXS experiments have been performed on actinides, particularly on uranium systems. Uranium has a partly filled 5f shell. Core levels that have been used in RIXS experiments are the 3d XAS (M4,5 edge) at 3,550 eV (M5 edge) and 3,728 eV (M4 edge), the 4d XAS at 778 eV (N4 edge) and the 5d XAS (O4,5 edge) at 110 eV. 5d5f valence RIXS was measured for UF4. High-resolution RIXS data can detect ff transitions that are affected by 5f5f electron–electron interactions, 5f spin–orbit coupling and crystal-field effects210. The spectra can be well simulated with the Anderson impurity model. The americium 5d5f RIXS shows a low-intense charge-transfer satellite in the americium 5d5f RIXS owing to americium 5f–oxygen 2p hybridization, as also predicted from the impurity model211. 5d5f RIXS shows that the curium oxide ground state configuration best describes as trivalent curium212. 3d5f valence RIXS was measured for a series of uranium oxides, in which the uranium 5f–oxygen 2p hybridization leads to specific charge-transfer peaks for each oxide213. 3d4f core RIXS planes were measured to determine the valency, 5f occupations and possible oxidation effects in uranyl214, early actinides215, actinide dioxides216 and uranium intermetallics217. The improved resolution of the IRIXS tender X-ray beamline enables detailed 3d5f RIXS experi- ments. Recent data on UGa2 show high-resolution multiplet features that give a new view on the combination of localization and itineracy in uranium

intermetallics218. At the soft X-ray RIXS beamline, high-resolution 4d5f RIXS of UO2 confirms the first excited state of the 3F2 multiplet at ~520 meV (ref. 219).

Molecular systems

For molecules, momentum transfer does not play a role and the focus is on RIXS experiments to measure vibrations and electronic excitations. A detailed overview of RIXS in atoms and molecules is given in ref. 48, in which resonant X-ray Raman is used as an alternative name for RIXS. The screening of core hole excitations is different in solids and molecules, suggesting that resonant and non-resonant IXS are also different.

For small molecules in the gas phase, for example, O2 or H2O, RIXS excited at the oxygen K edge XAS shows a series of sharp vibrational levels. The RIXS data on gas-phase H2O give a series of vibrational states, in which the number of states increases when the incident energy is on the high-energy side of an electronic XAS excitation47. Similar behaviour is observed in liquid H2O. In liquids, the higher states are broader, whereas in the gas phase they have the same broadening, as explained in detail with calculations in ref. 47. RIXS shows interesting phenomena when the incident energy is reduced stepwise to below a resonance, called detuning220–224. The Kramer–Heisenberg equation can be rewritten into a time analysis and the detuning related to a scattering duration time. This detuning effect can be used to distinguish bound states from dissociative states by the core hole clock mechanism225–227. This could be interpreted as an effect stemming from a difference in the decoherence times of these excitations.

Metal centres in complexes

Fluorescence yield XAS records data on samples with low absorber concentration and is ideal for measuring metal centres in proteins. The core excitation is specific to the metal and the low concentration prevents spectral distortions owing to energy-dependent probing depths and self-absorption. In addition, 1s2p RIXS measures spectra that look similar to 2p XAS, as shown for Fe2O3 (ref. 97). A comparison between 2p XAS and 1s2p RIXS was measured for a series of model iron systems with different valences, symmetries and the presence or absence of π-back-bonding. The multiplet analysis showed that 1s2p RIXS is more sensitive to σ-bonding, whereas 2p XAS has larger satellites owing to π-back-bonding228. The combination of 2p XAS and 1s2p RIXS is an important route for studying valency and covalency effects in protein metal centres, for example, 1s2p RIXS has been used to study the ground state of a Fe(IV) = O species229. Photosystem II has also been studied, in which its 1s2p RIXS spectra showed electronic structure changes on laser excitation from the S1 to S2 state230. An important feature of 1s XAS is that the pre-edge region is strongly enhanced if the inversion symmetry of the absorbing site is broken. For example, in tetrahedral symmetry, there is a strong mix- ing between local 3d and 4p states229,231. The valence-to-core X-ray emission arises from electrons in orbitals centred at the ligand positions. Combining valence-to-core XES with resonant excitation — in other words, valence RIXS — the selectivity of XES can be tuned to a specific ligand type232–234. 2p3d RIXS can also be applied to coordination complexes, despite the sensitivity to radiation damage. An example is the quantification of steric effects in iron carbene photosensitizers235.

Battery materials

Understanding the evolution of transition metal oxide cathodes is at the core of developing higher-energy density battery materials. Typically, the oxidation state of the transition metal ions is changed to compensate extraction and insertion of Li+ ions during the charge and discharge process. However, the energy capacity is hindered owing to limited oxidation or reduction of transition metal ions. In the new class of oxygen-redox cathode materials, higher voltage can be applied to oxidize both the transition metal and oxygen ions. However, the high voltage associated with oxidation of O − during the charge cannot recover on discharge, resulting in reduced energy density. Applying high-resolution RIXS at the oxygen K edge, a cascade of vibrational spectra was found in sodium-rich and lithium-rich cathode materials, whose frequency is identical to molecular O2 (refs. 236–239). The voltage loss on discharge can be understood by migration of the

transition metal ions and loss of oxidized molecular O2 escaping the cathodes. These studies provide a method of optimizing oxygen-redox cathodes for new-generation battery materials.

Time-resolved RIXS experiments

Pump–probe RIXS experiments can study the dynamics of RIXS excitations. An important group of pump–probe RIXS experiments is on liquid jet experiments. In liquid jet experiments, the sample is renewed at every X-ray pulse, making it possible to perform experiments on X-ray-sensitive systems, for example, the dissociation of Fe(CO)5. The valence 2p3d RIXS was measured at the iron L3 edge with time delays of 0.7–3.5 ps. This enabled the electronic structure changes of the dis- sociation pathway to be tracked[240]. The spectral shapes of molecular and liquid systems are complex as they are a mixture of ground state structural and core-excited state dynamical contributions. RIXS spectra of liquid methanol were measured to determine the dynamics of the O–H bond in the core excited state[241]. Light-induced C–H bond activation has been studied with rhodium 2p4d RIXS in a series of rhodium complexes[242].

Reproducibility and data deposition

Energy and intensity calibration

RIXS experiments use synchrotron beamlines with grating or crystal monochromators. Although it is possible to calibrate the monochromator and detector in absolute energies, this is not always undertaken owing to time constraints. The Xray energy is usually calibrated with published references. The absolute X-ray incident energy is not crucial for the RIXS data analysis. The only important energy calibration is the zero energy loss that is given by the position of the elastic scattering. The absolute intensity of an RIXS experiment is not usually measured. It is influenced by all beamline components, detector area and efficiency. The RIXS analysis is focused on relative intensities within a spectrum or RIXS plane.

Potential data distortions

RIXS uses high-intensity X-ray beams that can modify the sample. In all RIXS experiments, care must be taken to check for potential sample modifications. Because RIXS is a photon-in–photon-out experiment, the effects of sample damage are not as strong as in electron yield measurements owing to the larger probing depth. RIXS experiments can suffer from saturation and self-absorption effects[243]. Saturation effects occur owing to the energy-dependent penetration depth of X-rays through an X-ray absorption spectrum. Self-absorption effects occur owing to the absorption of emitted X-rays. Self-absorption is particularly important for near elastic X-ray emission that can be re-absorbed. Saturation and self-absorption effects disappear for diluted samples.

Data deposition

RIXS data are measured at synchrotron radiation sources. The data are usually stored based on the rules of each facility. Typically, raw image data are kept in the central storage for about 2–3 years, during which time users can access the data whenever required. Thereafter, data are moved to permanent tapes. Many large facilities are currently discussing the open data policy that means, after certain period of time, raw data should match the FAIR data principles of being findable, accessible, interoperable and reusable. The ESRF data policy has been implemented, in which data of publicly funded research are released to become open access for everyone after a 3-year embargo period.

Currently, no major data repository exists for X-ray spectroscopy. Several databases are available and efforts are underway to define standards, for instance, data format and metadata, to establish a widely accepted database similar to those available for crystal structures. However, this mainly concerns XAS and non-resonant XES. There is a limited amount of measured RIXS spectra and they have a range of different experimental parameters — including incident energy, emission energy, incident polarization, emission polarization, incident angle, emission angle and sample orientation — alongside sample parameters such as orientation,

texture and temperature. In practice, only a limited data set can be measured within the available beamtime and these data are focused on the specific research question.

Limitations and optimizations

Resolution and intensity

The intrinsic cross-section of RIXS experiments is low. The total cross- section is a combination of the XAS cross-section, the detection solid angle and the XES cross-section. For soft X-rays, the XAS cross-section is large but most core holes decay by more than 99% Auger decay, yielding a low XES cross-section. In addition, the solid angle of the XES detector is small. For hard X-rays, the XAS cross-section is small. Most core holes decay radiatively and the crystal detectors allow a relatively large solid angle. A low cross-section implies limitations with experiments that need a large intrinsic signal, for example, RIXS measurements of low-concentration samples and RIXS microscopy.

There is a balance between X-ray resolution and measured intensity. Higher-resolution experiments will have lower intensity. In soft X-ray RIXS, a 20 meV resolution needs more stringent boundary conditions on the solid angle of the XES spectrometer. On the same machine, a 100 meV resolution experiment will have considerably higher inten- sity. New developments with transition element sensors can measure XES with 500 meV resolution without the need for an XES monochroma- tor[244,245]. This enables higher intensity but does not allow high-resolution RIXS experiments. In hard X-ray RIXS with spherically bent crystals, the resolution is given by the scattering distance. The larger the distance, the higher the potential resolution but the lower the intensity. In prac- tice, resolution and intensity need to be optimized depending on the experimental goals, within the limits of each beamline.

Polarization and momentum transfer

Some RIXS beamlines have the choice of X-rays being circularly or horizontally polarized, but these options are not available at all beamlines. Only a few beamlines can detect the polarization of the emitted X-rays, which comes at the cost of reduced intensity. Momentum transfer is determined by the scattering angle. A limitation of soft X-ray RIXS is that the maximum momentum transfer reaches only a part of the Brillouin zone, meaning only partial mapping. Hard X-rays can fully map the Brillouin zone; however, hard X-ray RIXS at K edges has very low intensity as it needs quadrupole excitation and quadrupole decay. Band mapping with hard X-ray RIXS is possible at the L edges of 5d elements. Several experimental stations have been optimized for RIXS at the iridium L3 edge[200].

Outlook

The main driving force of future developments will be improvements in experiments, including increased energy and momentum resolution. Improved intensity and detectors will lead to increased overall count rates, enabling new experiments, including the development of RIXS microscopy. Newly designed reactor cells and dedicated sample environments will stimulate experiments under in situ or operando conditions. New beamlines at X-ray FELs will stimulate time-resolved and nonlinear experiments. This section briefly discusses new possibilities.

Resolution

Improved energy and momentum resolution, combined with higher count rates, will give a more complete mapping of the scattering function. A soft X-ray RIXS resolution of 5 meV, combined with good momen- tum resolution, will enable mapping of electron–hole excitation band structures, although the momentum transfer available with soft X-rays is not enough to map the whole Brillouin zone. In the hard X-ray range, this would lead to full Brillouin zone mapping. It is expected that the combination of good energy and momentum resolution will only be possible for L edges as it is unlikely that the quadrupole pre-edges at K edges will yield enough intensity. There is the potential alternative of resonant inelastic electron scattering, but very few experiments are being performed in that direction[246].

X-ray free electron lasers

Time. A major new set of data will appear from RIXS beamlines at XFEL sources. This includes pump–probe RIXS experiments of excited states and nonlinear X-ray spectroscopy experiments. Because RIXS is much more sensitive to electronic states than XAS, it is expected that the decay pathways can be pinpointed with higher precision. The Heisenberg RIXS end station at European XFEL is becoming available. This will combine femtosecond time-resolved and milli- electronvolt energy-resolved RIXS spectra down to the theoretical Fourier limit.

Nonlinear effects. Nonlinear effects occur when the X-ray intensity is high enough. This regime has been reached by X-ray FEL sources. This allows stimulated RIXS experiments, which gave an enhancement of approximately 106 in intensity for a Co/Pd multilayer at the cobalt 2p edge[247]. In the hard X-ray range, the 1s3p XES signal was enhanced with a two-colour X-ray experiment in which one pulse was used to invert the 1s population and a second pulse to amplify the 1s3p XES signal[248]. With the maturation of XFEL sources, experiments are expected with nonlinear effects and multiple X-ray energies.

Operando

Further developments of dedicated reactor cells and sample environments will improve operando studies for energy materials. Because intense X-ray beams are used, there is a trade-off with X-ray damage and X-ray-induced effects. As the tender X-ray region is more widely explored at synchrotrons, new applications will arise. RIXS increases the selectivity of the X-ray spectroscopy probe, which is important in the analysis of heterogeneous systems. The L edges of 4d transition metals are currently being explored, including operando studies in catalysis research. Only a few RIXS studies have looked at the K edges of sulfur and chlorine. These spectra contain a wealth of information and are more accessible to first-principle theoretical modelling because of weaker electron correlations compared with metal ions.

Polarization

An intriguing prospect is the use of twisted X-ray photon beams, also known as vortex. This approach uses X-rays that are not plane waves[249]. The wavefront of the photon beam is helical, indicating that the photons have non-zero orbital angular momentum $m\hbar$ — in which m is an integer called topological charge — along the wave vector. With this type of photon, it is possible to perform spectroscopic measurements that obey different electronic transition selection rules than those known with plane wave beams. This has been predicted for 3d and 4d ions in condensed matter, including cuprates, manganites and ruthenates[250]. An interesting effect is the possibility of measuring electric quadrupole transitions 1s → 3d in a pure way, not superimposed on the intense electric 1s → 4p dipole transitions, as occurs when measuring K edges with conventional X-beams. This technique could provide a reliable measure of the density of empty d-states, local site symmetry and orbital magnetic moment without needing to measure a full angular distribution map to remove the dipole part of the signal[251]. Furthermore, it has been proposed that the interaction between these photons and topologically complex materials — such as magnetic skyrmions or chiral materials — could help understand the origin of their properties[250] and possibly excite exotic states, such as twisted magnons[252]. It is expected that using twisted X-ray photon beams will gain popularity owing to the rise of X-ray sources with high transverse coherence and XFEL sources.

Microscopy and dilute systems

The improved intensity and X-ray beam characteristics of upgraded diffraction limited light sources will improve the combination of RIXS and X-ray microscopy. One option is to use an optical design that maps energy in one direction and position in a second direction on a 2D detector[253]. This will enable RIXS spectra to be collected on a line through a sample. Improved count rates will allow more experiments with weaker transitions, for example, impurity systems, molecular systems and thin films. RIXS has been occasionally applied to impurities, for example, ruby, which has Cr3+ impurities in Al2O3. Increased intensity will lead to applications in luminescent materials and other systems with low concentrations of 3d or 4f elements.

Summary

Over the past 20 years, valence RIXS has become a powerful technique owing to enormous improvements in energy resolution, from 1 eV down to 20 meV. This has enabled element-specific collective excitations to be measured in quantum materials. Combined with the polarization and momentum dependence of the measurements, this has created a new level of experimental observations. Core RIXS has not reached the same resolution, but does allow detailed experiments of energy materials under operando conditions in reactor cells. In the coming years, new experimental options at X-ray FELs will also add the study of femto-second time-resolved phenomena and nonlinear X-ray experiments to the RIXS toolbox.

References

1. Kunnus, K. et al. Anti-Stokes resonant X-ray Raman scattering for atom specific and excited state selective dynamics. *New J. Phys.* **18**, 103011 (2016).
2. de Groot, F., Vankó, G. & Glatzel, P. The 1*s* X-ray absorption pre-edge structures in transition metal oxides. *J. Phys. Condens. Matter* **21**, 104207 (2009).
3. de Groot, F. M. F. X-ray absorption and dichroism of transition metals and their compounds. *J. Electron. Spectros. Relat. Phenom.* **67**, 529 (1994).
4. van den Brink, J. & van Veenendaal, M. Theory of indirect resonant inelastic X-ray scattering. *J. Phys. Chem. Solids* **66**, 2145–2149 (2005).
5. van den Brink, J. & van Veenendaal, M. Correlation functions measured by indirect resonant inelastic X-ray scattering. *Europhys. Lett.* **73**, 121–127 (2006).
6. Hunault, M. O. J. Y. et al. Direct observation of Cr^{3+} 3*d* states in ruby: toward experimental mechanistic evidence of metal chemistry. *J. Phys. Chem. A* **122**, 4399–4413 (2018).
7. Ghiringhelli, G. et al. SAXES, a high resolution spectrometer for resonant X-ray emission in the 400–1,600 eV energy range. *Rev. Sci. Instrum.* **77**, 113108 (2006).
   Improvements in resonant inelastic X-ray scattering instruments.
8. Brookes, N. B. et al. The beamline ID32 at the ESRF for soft X-ray high energy resolution resonant inelastic X-ray scattering and polarisation dependent X-ray absorption spectroscopy. *Nucl. Instrum. Methods Phys. Res. Sect. A Accel. Spectrom. Detect. Assoc. Equip.* **903**, 175–192 (2018).
9. Zhou, K. J. et al. 121: an advanced high-resolution resonant inelastic X-ray scattering beamline at diamond light source. *J. Synchrotron Radiat.* **29**, 563–580 (2022).
10. Dvorak, J., Jarrige, I., Bisogni, V., Coburn, S. & Leonhardt, W. Towards 10 meV resolution: the design of an ultrahigh resolution soft X-ray RIXS spectrometer. *Rev. Sci. Instrum.* **87**, 115109 (2016).
11. Singh, A. et al. Development of the soft X-ray AGM-AGS RIXS beamline at the Taiwan photon source. *J. Synchrotron Radiat.* **28**, 977–986 (2021).
12. Braicovich, L. et al. The simultaneous measurement of energy and linear polarization of the scattered radiation in resonant inelastic soft X-ray scattering. *Rev. Sci. Instrum.* **85**, 115104 (2014).
13. Sala, M. M. et al. A high-energy-resolution resonant inelastic X-ray scattering spectrometer at ID20 of the European Synchrotron Radiation Facility. *J. Synchrotron Radiat.* **25**, 580 591 (2018).
14. Kramers, H. A. & Heisenberg, W. On the dispersal of radiation by atoms. *Z. Fur Phys.* **31**, 681–708 (1925).
15. Kubo, R. Statistical-mechanical theory of irreversible processes. 1. General theory and simple applications to magnetic and conduction problems. *J. Phys. Soc. Jpn.* **12**, 570–586 (1957).
16. Kubo, R., Yokota, M. & Nakajima, S. Statistical-mechanical theory of irreversible processes. 2. Response to thermal disturbance. *J. Phys. Soc. Jpn.* **12**, 1203–1211 (1957).
17. de Groot, F. & Kotani, A. *Core Level Spectroscopy of Solids*. *Core Level Spectroscopy of Solids* (CRC Press, 2008).
18. Winfried, S. *Electron Dynamics by Inelastic X-Ray Scattering* (Oxford Univ. Press, 2007).
19. Schlappa, J. et al. Collective magnetic excitations in the spin ladder $Sr_{14}Cu_{24}O_{41}$ measured using high-resolution resonant inelastic X-ray scattering. *Phys. Rev. Lett.* **103**, 047401 (2009).
20. Braicovich, L. et al. Dispersion of magnetic excitations in the cuprate La_2CuO_4 and $CaCuO_2$ compounds measured using resonant X-ray scattering. *Phys. Rev. Lett.* **102**, 167401 (2009).
21. Le Tacon, M. et al. Intense paramagnon excitations in a large family of high-temperature superconductors. *Nat. Phys.* **7**, 725–730 (2011).
22. Kim, J. et al. Magnetic excitation spectra of Sr_2IrO_4 probed by resonant inelastic X-ray scattering: establishing links to cuprate superconductors. *Phys. Rev. Lett.* **108**, 177003 (2012).
    Hard X-ray resonant inelastic X-ray scattering experiment on iridates.
23. Zhou, K.-J. et al. Persistent high-energy spin excitations in iron-pnictide superconductors. *Nat. Commun.* **4**, 1470 (2013).
24. Haverkort, M. W. Theory of resonant inelastic X-ray scattering by collective magnetic excitations. *Phys. Rev. Lett.* **105**, 167404 (2010).
25. Glawion, S. et al. Two-spinon and orbital excitations of the spin-Peierls system. *Phys. Rev. Lett.* **107**, 107402 (2011).
26. Schlappa, J. et al. Spin-orbital separation in the quasi-one-dimensional Mott insulator Sr_2CuO_3. *Nature* **485**, 82–85 (2012).
    Low-energy excitations in cuprates (spinons and orbitons).
27. Benckiser, E. et al. Orbital superexchange and crystal field simultaneously at play in YVO_3: resonant inelastic X-ray scattering at the V *L* edge and the O *K* edge. *Phys. Rev. B* **88**, 205115 (2013).
28. Nomura, T. et al. Resonant inelastic X-ray scattering study of entangled spin-orbital excitations in superconducting $PrFeAsO_{0.7}$. *Phys. Rev. B* **94**, 035134 (2016).
29. Wang, R. P. et al. Excitonic dispersion of the intermediate spin state in $LaCoO_3$ revealed by resonant inelastic X-ray scattering. *Phys. Rev. B* **98**, 1–6 (2018).
30. Moser, S. et al. Electron–phonon coupling in the bulk of anatase TiO_2 measured by resonant inelastic X-ray spectroscopy. *Phys. Rev. Lett.* **115**, 096404 (2015).
31. Ament, L. J. P., van Veenendaal, M. & van den Brink, J. Determining the electron–phonon coupling strength from resonant inelastic X-ray scattering at transition metal L-edges. *epl* **95**, 27008 (2011).
32. Bieniasz, K., Johnston, S. & Berciu, M. Theory of dispersive optical phonons in resonant inelastic X-ray scattering experiments. *Phys. Rev. B* **105**, L180302 (2022).
33. Ueda, H. et al. Chiral phonons in quartz probed by X-rays. *Nature* **618**, 946 (2023).
34. Chaix, L. et al. Dispersive charge density wave excitations in $Bi_2Sr_2CaCu_2O_{8+\delta}$. *Nat. Phys.* **13**, 952 (2017).
35. da Silva Neto, E. H. et al. Coupling between dynamic magnetic and charge-order correlations in the cuprate superconductor $Nd_{2-x}Ce_xCuO_4$. *Phys. Rev. B* **98**, 161114(R) (2018).
36. Boschini, F. et al. Dynamic electron correlations with charge order wavelength along all directions in the copper oxide plane. *Nat. Commun.* **12**, 597 (2021).
37. Tam, C. C. et al. Charge density waves and Fermi surface reconstruction in the clean overdoped cuprate superconductor $Tl_2Ba_2CuO_{6+\delta}$. *Nat. Commun.* **13**, 570 (2022).
38. Miao, H. et al. Charge density waves in cuprate superconductors beyond the critical doping. *npj Quantum Mater.* **6**, 31 (2021).
39. Porter, Z. et al. Spin–orbit excitons and electronic configuration of the $5d^4$ insulator $Sr_3Ir_2O_7F_2$. *Phys. Rev. B* **106**, 115140 (2022).
40. Das, L. et al. Spin–orbital excitations in Ca_2RuO_4 revealed by resonant inelastic X-ray scattering. *Phys. Rev. X* **8**, 011048 (2018).
41. Hill, J. P. et al. Observation of a 500 meV collective mode in $La_{2-x}Sr_xCuO_4$ and Nd_2CuO_4 using resonant inelastic X-ray scattering. *Phys. Rev. Lett.* **100**, 097001 (2008).
42. Nag, A. et al. Many-body physics of single and double spin-flip excitations in NiO. *Phys. Rev. Lett.* **124**, 067202 (2020).
43. Li, J. et al. Single- and multimagnon dynamics in antiferromagnetic α-Fe_2O_3 thin films. *Phys. Rev. X* **13**, 011012 (2023).
44. Elnaggar, H. et al. Magnetic excitations beyond the single- and double-magnons. *Nat. Commun.* **14**, 2749 (2023).
45. Betto, D. et al. Multiple-magnon excitations shape the spin spectrum of cuprate parent compounds. *Phys. Rev. B* **103**, 011012 (2021).
46. Savchenko, V. et al. Vibrational resonant inelastic X-ray scattering in liquid acetic acid: a ruler for molecular chain lengths. *Sci. Rep.* **11**, 4098 (2021).
47. Pietzsch, A. et al. Cuts through the manifold of molecular H_2O potential energy surfaces in liquid water at ambient conditions. *Proc. Natl Acad. Sci. USA* **119**, e2118101119 (2022).
48. Gel'mukhanov, F. & Agren, H. Resonant X-ray Raman scattering. *Phys. Rep. Rev. Sect. Phys. Lett.* **312**, 87–330 (1999).
49. Butorin, S. M. et al. Resonant X-ray fluorescence spectroscopy of correlated systems: a probe of charge-transfer excitations. *Phys. Rev. Lett.* **77**, 574–577 (1996).
50. Luo, J., Trammell, G. T. & Hannon, J. P. Scattering operator for elastic and inelastic resonant X-ray-scattering. *Phys. Rev. Lett.* **71**, 287–290 (1993).
51. Ament, L. J. P., Ghiringhelli, G., Moretti Sala, M., Braicovich, L. & van den Brink, J. Theoretical demonstration of how the dispersion of magnetic excitations in cuprate compounds can be determined using resonant inelastic X-ray scattering. *Phys. Rev. Lett.* **103**, 117003 (2009).
52. Haverkort, M. W., Hollmann, N., Krug, I. P. & Tanaka, A. Symmetry analysis of magneto-optical effects: the case of X-ray diffraction and X-ray absorption at the transition metal $L_{2,3}$ edge. *Phys. Rev. B Condens. Matter Mater. Phys.* **82**, 094403 (2010).

53. Lu, Y. & Haverkort, M. W. Nonperturbative series expansion of Green's functions: the anatomy of resonant inelastic X-ray scattering in the doped Hubbard model. *Phys. Rev. Lett.* **119**, 256401 (2017).
54. Kang, M. et al. Resolving the nature of electronic excitations in resonant inelastic X-ray scattering. *Phys. Rev. B* **99**, 045105 (2019).
55. Jia, C., Wohlfeld, K., Wang, Y., Moritz, B. & Devereaux, T. P. Using RIXS to uncover elementary charge and spin excitations. *Phys. Rev. X* **6**, 021020 (2016).
56. Jiménez-Mier, J. et al. Dynamical behavior of X-ray absorption and scattering at the *L* edge of titanium compounds: experiment and theory. *Phys. Rev. B* **59**, 2649–2658 (1999).
57. de Groot, F., Sawatzky, G. & Kuiper, P. Local spin-flip spectral distribution obtained by resonant X-ray Raman scattering. *Phys. Rev. B Condens. Matter Mater. Phys.* **57**, 14584–14587 (1998).

Prediction of magnetic excitations.

58. Lee, S., Zhai, H. & Chan, G. K.-L. An ab initio correction vector restricted active space approach to the *L*-edge XAS and 2*p*3*d* RIXS spectra of transition metal complexes. *J. Chem. Theory Comput.* **19**, 7753–7763 (2023).
59. Werner, P., Johnston, S. & Eckstein, M. Nonequilibrium-DMFT based RIXS investigation of the two-orbital Hubbard model. *epl* **133**, 57005 (2021).
60. Hariki, A., Winder, M., Uozumi, T. & Kunes, J. LDA plus DMFT approach to resonant inelastic X-ray scattering in correlated materials. *Phys. Rev. B* **101**, 115130 (2020).
61. Haverkort, M. W. Quanty for core level spectroscopy — excitons, resonances and band excitations in time and frequency domain. *J. Phys. Conf. Ser.* **712**, 12001 (2016).
62. Wang, S.-X. & Zhu, L.-F. Non-resonant inelastic X-ray scattering spectroscopy: a momentum probe to detect the electronic structures of atoms and molecules. *Matter Radiat. Extrem.* **5**, 054201 (2020).
63. Schülke, W. Electronic excitations investigated by inelastic X-ray scattering spectroscopy. *J. Phys. Condens. Matter* **13**, 7557–7591 (2001).
64. Krisch, M. & Sette, F. Inelastic X-ray scattering from phonons. in *Light Scattering in Solids IX: Novel Materials and Techniques* Vol. 108 (eds Cardona, M. & Merlin, R.) 317–369 (Springer, 2007).
65. Nelayah, J. et al. Mapping surface plasmons on a single metallic nanoparticle. *Nat. Phys.* **3**, 348–353 (2007).
66. Pintschovius, L. Electron–phonon coupling effects explored by inelastic neutron scattering. *Phys. Status Sol. B Basic Solid State Phys.* **242**, 30–50 (2005).
67. Rossatmignod, J. et al. Investigation of the spin dynamics in $YBa_2Cu_3O_{6+x}$ by inelastic neutron-scattering. *Phys. B* **169**, 58–65 (1991).
68. Damascelli, A. Probing the electronic structure of complex systems by ARPES. *Phys. Scr.* **T109**, 61–74 (2004).
69. Cuk, T. et al. A review of electron–phonon coupling seen in the high-T_c superconductors by angle-resolved photoemission studies (ARPES). *Phys. Status Sol. B Basic Solid State Phys.* **242**, 11–29 (2005).
70. Abanov, A. & Chubukov, A. V. A relation between the resonance neutron peak and ARPES data in cuprates. *Phys. Rev. Lett.* **83**, 1652–1655 (1999).
71. Kotani, A. Resonant inelastic X-ray scattering in *d* and *f* electron systems. *Eur. Phys. J. B* **47**, 3–27 (2005).
72. Hepting, M., Dean, M. P. M. & Lee, W. S. Soft X-ray spectroscopy of low-valence nickelates. *Front. Phys.* **9**, 808683 (2021).
73. Cao, Y. et al. Ultrafast dynamics of spin and orbital correlations in quantum materials: an energy- and momentum-resolved perspective. *Philos. Trans. R. Soc. A Math. Phys. Eng. Sci.* **377**, 20170480 (2019).
74. Baker, M. L. et al. K- and L-edge X-ray absorption spectroscopy (XAS) and resonant inelastic X-ray scattering (RIXS) determination of differential orbital covalency (DOC) of transition metal sites. *Coord. Chem. Rev.* **345**, 182–208 (2017).
75. Monney, C., Patthey, L., Razzoli, E. & Schmitt, T. Static and time-resolved resonant inelastic X-ray scattering: recent results and future prospects. *X-Ray Spectrom.* **52**, 216–225 (2023).
76. Ament, L. J. P., van Veenendaal, M., Devereaux Thomas, P., Hill, J. P. & van den Brink, J. Resonant inelastic X-ray scattering studies of elementary excitations. *Rev. Mod. Phys.* **83**, 705 (2011).
77. Glatzel, P. & Bergmann, U. High resolution 1*s* core hole X-ray spectroscopy in 3*d* transition metal complexes — electronic and structural information. *Coord. Chem. Rev.* **249**, 65–95 (2005).
78. Glatzel, P., de Groot, F. M. F. & Bergmann, U. Hard X-ray photon-in photon-out spectroscopy. *Synchrotron Radiat. News* **22**, 12–16 (2009).
79. De Groot, F. High-resolution X-ray emission and X-ray absorption spectroscopy. *Chem. Rev.* **101**, 1779–1808 (2001).
80. Gel'mukhanov, F. Theory of resonant inelastic X-ray scattering (RIXS) spectra. *J. Electron. Spectros. Relat. Phenom.* **156**, XXI (2007).
81. Gel'mukhanov, F., Odelius, M., Polyutov, S. P., Foehlisch, A. & Kimberg, V. Dynamics of resonant X-ray and Auger scattering. *Rev. Mod. Phys.* **93**, 035001 (2021).
82. Kotani, A. & Shin, S. Resonant inelastic X-ray scattering spectra for electrons in solids. *Rev. Mod. Phys.* **73**, 203–246 (2001).
83. Huotari, S. et al. Improving the performance of high-resolution X-ray spectrometers with position-sensitive pixel detectors. *J. Synchrotron Radiat.* **12**, 467–472 (2005).
84. Gretarsson, H. et al. IRIXS: a resonant inelastic X-ray scattering instrument dedicated to X-rays in the intermediate energy range. *J. Synchrotron Radiat.* **27**, 538–544 (2020).
85. Bertinshaw, J. et al. IRIXS spectrograph: an ultra high-resolution spectrometer for tender RIXS. *J. Synchrotron Radiat.* **28**, 1184–1192 (2021).
86. Kuiper, P. et al. Resonant X-ray Raman spectra of Cu *dd* excitations in Sr(2)CuO(2)Cl(2). *Phys. Rev. Lett.* **80**, 5204–5207 (1998).
87. Chuang, Y. D. et al. High-resolution soft X-ray emission spectrograph at advanced light source. *J. Phys. Chem. Solids* **66**, 2173–2178 (2005).
88. Wray, L. A., Yang, W. L., Eisaki, H., Hussain, Z. & Chuang, Y. D. Multiplet resonance lifetimes in resonant inelastic X-ray scattering involving shallow core levels. *Phys. Rev. B* **86**, 195130 (2012).
89. Chiuzbaian, S. G. et al. Localized electronic excitations in NiO studied with resonant inelastic X-ray scattering at the Ni M threshold: evidence of spin flip. *Phys. Rev. Lett.* **95**, 197402 (2005).
90. Bauer, K. et al. The meV XUV-RIXS facility at UE112-PGM1 of BESSY II. *J. Synchrotron Radiat.* **29**, 908–915 (2022).
91. Ellis, D. S. et al. Electronic structure of doped lanthanum cuprates studied with resonant inelastic X-ray scattering. *Phys. Rev. B* **83**, 075120 (2011).
92. Kim, Y.-J. et al. Observations on the resonant inelastic X-ray scattering cross section in copper oxide compounds. *Phys. Rev. B* **76**, 155116 (2007).
93. Chabot-Couture, G. et al. Polarization dependence and symmetry analysis in indirect *K*-edge RIXS. *Phys. Rev. B* **82**, 035113 (2010).
94. Kotani, A., Kvashnina, K. O., Butorin, S. M. & Glatzel, P. Spectator and participator processes in the resonant photon-in and photon-out spectra at the Ce *L*-3 edge of CeO_2. *Eur. Phys. J. B* **85**, 257 (2012).
95. Kas, J. J., Rehr, J. J., Soininen, J. A. & Glatzel, P. Real-space Green's function approach to resonant inelastic X-ray scattering. *Phys. Rev. B* **83**, 235114 (2011).
96. Bagger, A. et al. 1*s*2*p* resonant inelastic X-ray scattering combined dipole and quadrupole analysis method. *J. Synchrotron Radiat.* **24**, 296–301 (2017).
97. Caliebe, W., Kao, C., Hastings, J., Taguchi, M. & Kotani, A. Resonant inelastic X-ray scattering. *Phys. Rev. B* **58**, 13452–13458 (1998).
98. Kurian, R., van Schooneveld, M. M., Zoltán, N., Vankó, G. & de Groot, F. M. F. Temperature-dependent 1*s*2*p* resonant inelastic X-ray scattering of CoO. *J. Phys. Chem. C* **117**, 2976–2981 (2013).
99. Rubensson, J., Eisebitt, S., Nicodemus, M., Boske, T. & Eberhardt, W. Exchange-split Ca 3*s*-13*d* states in CaF_2 observed in threshold excited core-to-core fluorescence. *Phys. Rev. B* **49**, 1507–1510 (1994).
100. Rubensson, J. E., Eisebitt, S., Nicodemus, M., Boske, T. & Eberhardt, W. Electron correlation in CaF_2 studied in threshold-excited soft-X-ray fluorescence. *Phys. Rev. B* **50**, 9035–9045 (1994).
101. de Groot, F. 3*s*2*p* inelastic X-ray scattering. *Phys. Rev. B Condens. Matter Mater. Phys.* **53**, 7099 (1996).
102. Kurian, R. et al. Intrinsic deviations in fluorescence yield detected X-ray absorption spectroscopy: the case of the transition metal $L_{2,3}$ edges. *J. Phys. Condens. Matter* **24**, 452201 (2012).
103. Hamalainen, K., Siddons, D. P., Hastings, J. B. & Berman, L. E. Elimination of the inner-shell lifetime broadening in X-ray-absorption spectroscopy. *Phys. Rev. Lett.* **67**, 2850–2853 (1991).

Removal of lifetime broadening in resonant inelastic X-ray scattering.

104. Carra, P., Fabrizio, M. & Thole, B. T. High resolution X-ray resonant Raman scattering. *Phys. Rev. Lett.* **74**, 3700–3703 (1995).
105. Glatzel, P. et al. Reflections on hard X-ray photon-in/photon-out spectroscopy for electronic structure studies. *J. Electron. Spectros. Relat. Phenom.* **188**, 17–25 (2013).
106. Kvashnina, K. O. & Butorin, S. M. High-energy resolution X-ray spectroscopy at actinide $M_{4,5}$ and ligand *K* edges: what we know, what we want to know, and what we can know. *Chem. Commun.* **58**, 327–342 (2022).
107. Kvashnina, K. O. et al. Chemical state of complex uranium oxides. *Phys. Rev. Lett.* **111**, 253002 (2013).

Resonant inelastic X-ray scattering application to actinides.

108. Blachucki, W. et al. High energy resolution off-resonant spectroscopy for X-ray absorption spectra free of self-absorption effects. *Phys. Rev. Lett.* **112**, 173003 (2014).
109. Glatzel, P., Jacquamet, L., Bergmann, U., De Groot, F. M. F. & Cramer, S. P. Site-selective EXAFS in mixed-valence compounds using high-resolution fluorescence detection: a study of iron in Prussian blue. *Inorg. Chem.* **41**, 3121–3127 (2002).
110. De Groot, F. M. F. et al. Local-spin-selective X-ray absorption and X-ray magnetic circular dichroism of MnP. *Phys. Rev. B* **51**, 1045 (1995).
111. Hämäläinen, K. et al. Spin-dependent X-ray absorption of MnO and MnF_2. *Phys. Rev. B* **46**, 14274–14277 (1992).
112. Pirngruber, G. D. et al. On the presence of Fe(IV) in Fe-ZSM-5 and $FeSrO_{3-x}$ — unequivocal detection of the 3*d*(4) spin system by resonant inelastic X-ray scattering. *J. Phys. Chem. B* **110**, 18104–18107 (2006).
113. Braicovich, L. et al. Magnetic circular dichroism in resonant Raman scattering in the perpendicular geometry at the *L* edge of 3*d* transition metal systems. *Phys. Rev. Lett.* **82**, 1566–1569 (1999).
114. Sikora, M. et al. Strong *K*-edge magnetic circular dichroism observed in photon-in– photon-out spectroscopy. *Phys. Rev. Lett.* **105**, 037202 (2010).

115. Miyawaki, J. et al. Dzyaloshinskii–Moriya interaction in alpha-Fe_2O_3 measured by magnetic circular dichroism in resonant inelastic soft X-ray scattering. *Phys. Rev. B* **96**, 214420 (2017).
116. Zhang, W. et al. Unraveling the nature of spin excitations disentangled from charge contributions in a doped cuprate superconductor. *npj Quantum Mater.* **7**, 123 (2022).
117. Sikora, M. et al. 1*s*2*p* resonant inelastic X-ray scattering-magnetic circular dichroism: a sensitive probe of 3*d* magnetic moments using hard X-ray photons. *J. Appl. Phys.* **111**, 123 (2012).
118. Lafuerza, S. et al. New reflections on hard X-ray photon-in/photon-out spectroscopy. *Nanoscale* **12**, 16270–16284 (2020).
119. Daffe, N. et al. Bad neighbour, good neighbour: how magnetic dipole interactions between soft and hard ferrimagnetic nanoparticles affect macroscopic magnetic properties in ferrofluids. *Nanoscale* **12**, 11222–11231 (2020).
120. Elnaggar, H. et al. Possible absence of trimeron correlations above the Verwey temperature in Fe_3O_4. *Phys. Rev. B* **101**, 085107 (2020).
121. Elnaggar, H. et al. Magnetic contrast at spin-flip excitations: an advanced X-ray spectroscopy tool to study magnetic-ordering. *ACS Appl. Mater. Interfaces* **11**, 36213–36220 (2019).
122. Minola, M. et al. Collective nature of spin excitations in superconducting cuprates probed by resonant inelastic X-ray scattering. *Phys. Rev. Lett.* **114**, 217003 (2015).
123. Fumagalli, R. et al. Polarization-resolved Cu L_3-edge resonant inelastic X-ray scattering of orbital and spin excitations in $NdBa_2Cu_3O_{7-\delta}$. *Phys. Rev. B* **99**, 134517 (2019).
124. Inami, T. Magnetic circular dichroism in X-ray emission from ferromagnets. *Phys. Rev. Lett.* **119**, 137203 (2017).
125. Ghiringhelli, G. & Braicovich, L. Magnetic excitations of layered cuprates studied by RIXS at Cu *L*3 edge. *J. Electron. Spectros. Relat. Phenom.* **188**, 26–31 (2013).
126. Ghiringhelli, G. et al. Low energy electronic excitations in the layered cuprates studied by copper L_3 resonant inelastic X-ray scattering. *Phys. Rev. Lett.* **92**, 117406 (2004).
127. Moretti Sala, M. et al. Energy and symmetry of *dd* excitations in undoped layered cuprates measured by Cu L_3 resonant inelastic X-ray scattering. *New J. Phys.* **13**, 043026 (2011).
128. Braicovich, L. et al. Magnetic excitations and phase separation in the underdoped $La_{2-x}Sr_xCuO_4$ superconductor measured by resonant inelastic X-ray scattering. *Phys. Rev. Lett.* **104**, 077002 (2010).

Resonant inelastic X-ray scattering experiment showing magnetic excitations.

129. Dean, M. P. M. et al. Persistence of magnetic excitations in $La_{2-x}Sr_xCuO_4$ from the undoped insulator to the heavily overdoped non-superconducting metal. *Nat. Mater.* **12**, 1019–1023 (2013).
130. Braicovich, L. et al. Momentum and polarization dependence of single-magnon spectral weight for Cu *L*3-edge resonant inelastic X-ray scattering from layered cuprates. *Phys. Rev. B Condens. Matter Mater. Phys.* **81**, 174533 (2010).
131. Dean, M. P. M. Insights into the high temperature superconducting cuprates from resonant inelastic X-ray scattering. *J. Magn. Magn. Mater.* **376**, 3–13 (2015).
132. Peng, Y. Y. et al. Influence of apical oxygen on the extent of in-plane exchange interaction in cuprate superconductors. *Nat. Phys.* **13**, 1201 (2017).
133. Wang, L. et al. Paramagnons and high-temperature superconductivity in a model family of cuprates. *Nat. Commun.* **13**, 3163 (2022).
134. Schlappa, J. et al. Probing multi-spinon excitations outside of the two-spinon continuum in the antiferromagnetic spin chain cuprate Sr_2CuO_3. *Nat. Commun.* **9**, 5394 (2018).
135. Bisogni, V. et al. Bimagnon studies in cuprates with resonant inelastic X-ray scattering at the O *K* edge. I. Assessment on La_2CuO_4 and comparison with the excitation at Cu L_3 and Cu *K* edges. *Phys. Rev. B* **85**, 214527 (2012).
136. Kumar, U. et al. Unraveling higher-order contributions to spin excitations probed using resonant inelastic X-ray scattering. *Phys. Rev. B* **106**, L060406 (2022).
137. Martinelli, L. et al. Fractional spin excitations in the infinite-layer cuprate $CaCuO_2$. *Phys. Rev. X* **12**, 021041 (2022).
138. Comin, R. & Damascelli, A. Resonant X-ray scattering studies of charge order in cuprates. *Annu. Rev. Condens. Matter Phys.* **7**, 369–405 (2016).
139. Arpaia, R. et al. Dynamical charge density fluctuations pervading the phase diagram of a Cu-based high-T_c superconductor. *Science* **365**, 906 (2019).
140. Ghiringhelli, G. et al. Long-range incommensurate charge fluctuations in (Y,Nd) $Ba_2Cu_3O_{6+x}$. *Science* **337**, 821–825 (2012).

Low-energy excitations in cuprates (charge fluctuations).

141. Arpaia, R. et al. Signature of quantum criticality in cuprates by charge density fluctuations. *Nat. Commun.* **14**, 7198 (2023).
142. Lee, W. S. et al. Spectroscopic fingerprint of charge order melting driven by quantum fluctuations in a cuprate. *Nat. Phys.* **17**, 53 (2021).
143. Li, J. M. et al. Multiorbital charge-density wave excitations and concomitant phonon anomalies in $Bi_2Sr_2LaCuO_{6+\delta}$. *Proc. Natl Acad. Sci. USA* **117**, 16219–16225 (2020).
144. Singh, A. et al. Unconventional exciton evolution from the pseudogap to superconducting phases in cuprates. *Nat. Commun.* **13**, 7906 (2022).
145. Hepting, M. et al. Three-dimensional collective charge excitations in electron-doped copper oxide superconductors. *Nature* **563**, 374 (2018).
146. Nag, A. et al. Detection of acoustic plasmons in hole-doped lanthanum and bismuth cuprate superconductors using resonant inelastic X-ray scattering. *Phys. Rev. Lett.* **125**, 257002 (2020).
147. Lin, J. et al. Doping evolution of the charge excitations and electron correlations in electron-doped superconducting $La_{2-x}Ce_xCuO_4$. *npj Quantum Mater.* **5**, 4 (2020).
148. Singh, A. et al. Acoustic plasmons and conducting carriers in hole-doped cuprate superconductors. *Phys. Rev. B* **105**, 235105 (2022).
149. Hepting, M. et al. Evolution of plasmon excitations across the phase diagram of the cuprate superconductor $La_{2-x}Sr_xCuO_4$. *Phys. Rev. B* **107**, 214516 (2023).
150. Hepting, M. et al. Gapped collective charge excitations and interlayer hopping in cuprate superconductors. *Phys. Rev. Lett.* **129**, 047001 (2022).
151. Saitoh, E. et al. Observation of orbital waves as elementary excitations in a solid. *Nature* **410**, 180–183 (2001).
152. Kim, C. et al. Observation of spin-charge separation in one-dimensional $SrCuO_2$. *Phys. Rev. Lett.* **77**, 4054–4057 (1996).
153. Martinelli, L. et al. Collective nature of orbital excitations in layered cuprates in the absence of apical oxygens. *Phys. Rev. Lett.* **132**, 066004 (2024).
154. Ge, J.-F. et al. Superconductivity above 100 K in single-layer FeSe films on doped $SrTiO_3$. *Nat. Mater.* **14**, 285–289 (2015).
155. Yang, W. L. et al. Evidence for weak electronic correlations in iron pnictides. *Phys. Rev. B* **80**, 014508 (2009).
156. Pelliciari, J. et al. Intralayer doping effects on the high-energy magnetic correlations in NaFeAs. *Phys. Rev. B* **93**, 134515 (2016).
157. Pelliciari, J. et al. Magnetic moment evolution and spin freezing in doped $BaFe_2As_2$. *Sci. Rep.* **7**, 8003 (2017).
158. Lu, X. et al. Spin-excitation anisotropy in the nematic state of detwinned FeSe. *Nat. Phys.* **18**, 806 (2022).
159. Pelliciari, J. et al. Evolution of spin excitations from bulk to monolayer FeSe. *Nat. Commun.* **12**, 3122 (2021).
160. Alonso, J. A., Martínez-Lope, M. J., Casais, M. T., Aranda, M. A. G. & Fernández-Díaz, M. T. Metal–insulator transitions, structural and microstructural evolution of $RNiO_3$ (R = Sm, Eu, Gd, Dy, Ho, Y) perovskites: evidence for room-temperature charge disproportionation in monoclinic $HoNiO_3$ and $YNiO_3$. *J. Am. Chem. Soc.* **121**, 4754–4762 (1999).
161. Cheong, S. W. et al. Charge-ordered states in $(La,Sr)_2NiO_4$ for hole concentrations n(h) = 1/3 and n(h) = 1/2. *Phys. Rev. B* **49**, 7088–7091 (1994).
162. Freeman, P. G. et al. Spin dynamics of half-doped $La_{3/2}Sr_{1/2}NiO_4$. *Phys. Rev. B* **71**, 174412 (2005).
163. Li, D. et al. Superconducting dome in $Nd_{1-x}Sr_xNiO_2$ infinite layer films. *Phys. Rev. Lett.* **125**, 027001 (2020).
164. Li, D. et al. Superconductivity in an infinite-layer nickelate. *Nature* **572**, 624 (2019).
165. Sun, H. et al. Signatures of superconductivity near 80 K in a nickelate under high pressure. *Nature* **621**, 493 (2023).
166. Fabbris, G. et al. Doping dependence of collective spin and orbital excitations in the spin-1 quantum antiferromagnet $La_{2-x}Sr_xNiO_4$ observed by X rays. *Phys. Rev. Lett.* **118**, 156402 (2017).
167. Bisogni, V. et al. Ground-state oxygen holes and the metal–insulator transition in the negative charge-transfer rare-earth nickelates. *Nat. Commun.* **7**, 13017 (2016).
168. Lu, Y. et al. Site-selective probe of magnetic excitations in rare-earth nickelates using resonant inelastic X-ray scattering. *Phys. Rev. X* **8**, 031014 (2018).
169. Hepting, M. et al. Electronic structure of the parent compound of superconducting infinite-layer nickelates. *Nat. Mater.* **19**, 381 (2020).
170. Lu, H. et al. Magnetic excitations in infinite-layer nickelates. *Science* **373**, 213–216 (2021).
171. Rossi, M. et al. Universal orbital and magnetic structures in infinite-layer nickelates. *Phys. Rev. B* **109**, 024512 (2024).
172. Lin, J. Q. et al. Strong superexchange in a $d^{9-\delta}$ nickelate revealed by resonant inelastic X-ray scattering. *Phys. Rev. Lett.* **126**, 087001 (2021).
173. Shen, Y. et al. Role of oxygen states in the low valence nickelate $La_4Ni_3O_8$. *Phys. Rev. X* **12**, 011055 (2022).
174. Shen, Y. et al. Electronic character of charge order in square-planar low-valence nickelates. *Phys. Rev. X* **13**, 011021 (2023).
175. Tam, C. C. et al. Charge density waves in infinite-layer $NdNiO_2$ nickelates. *Nat. Mater.* **21**, 1116 (2022).
176. Krieger, G. et al. Charge and spin order dichotomy in $NdNiO_2$ driven by the capping layer. *Phys. Rev. Lett.* **129**, 027002 (2022).
177. Rossi, M. et al. A broken translational symmetry state in an infinite-layer nickelate. *Nat. Phys.* **18**, 869 (2022).
178. Parzyck, C. T. et al. Absence of $3a_0$ charge density wave order in the infinite-layer nickelate $NdNiO_2$. *Nat. Mater.* **23**, 440 (2024).
179. Chen, X. et al. Electronic and magnetic excitations in $La_3Ni_2O_7$. Preprint at https:// arxiv.org/abs/2401.12657 (2024).
180. Nag, A. et al. Quadrupolar magnetic excitations in an isotropic spin-1 antiferromagnet. *Nat. Commun.* **13**, 2327 (2022).
181. Bernevig, B. A., Felser, C. & Beidenkopf, H. Progress and prospects in magnetic topological materials. *Nature* **603**, 41–51 (2022).
182. Yin, J.-X., Lian, B. & Hasan, M. Z. Topological kagome magnets and superconductors. *Nature* **612**, 647–657 (2022).
183. Nag, A. et al. Correlation driven near-flat band Stoner excitations in a Kagome magnet. *Nat. Commun.* **13**, 7317 (2022).
184. Brookes, N. B. et al. Spin waves in metallic iron and nickel measured by soft X-ray resonant inelastic scattering. *Phys. Rev. B* **102**, 064412 (2020).
185. Poelchen, G. et al. Long-lived spin waves in a metallic antiferromagnet. *Nat. Commun.* **14**, 5422 (2023).
186. Pelliciari, J. et al. Tuning spin excitations in magnetic films by confinement. *Nat. Mater.* **20**, 188 (2021).

187. von Arx, K. et al. Resonant inelastic X-ray scattering study of $Ca_3Ru_2O_7$. *Phys. Rev. B* **102**, 235104 (2020).
188. Lebert, B. W. et al. Resonant inelastic X-ray scattering study of α-$RuCl_3$: a progress report. *J. Phys. Condens. Matter* **32**, 144001 (2020).
189. Occhialini, C. A. et al. Local electronic structure of rutile RuO_2. *Phys. Rev. Res.* **3**, 033214 (2021).
190. Yang, Z. et al. Resonant inelastic X-ray scattering from electronic excitations in α-$RuCl_3$ nanolayers. *Phys. Rev. B* **108**, L041406 (2023).
191. Suzuki, H. et al. Spin waves and spin-state transitions in a ruthenate high-temperature antiferromagnet. *Nat. Mater.* **18**, 563–567 (2019).
Tender X-ray resonant inelastic X-ray scattering experiment on spin transitions.
192. Takahashi, H. et al. Nonmagnetic *J*=0 state and spin–orbit excitations in K_2RuCl_6. *Phys. Rev. Lett.* **127**, 227201 (2021).
193. Qamar, A. et al. Experimental and theoretical characterization of X-ray induced excitons, magnons, and *dd* transitions in MoO_3 nanosheets. *Phys. Rev. Mater.* **6**, 074003 (2022).
194. Biasin, E. et al. Revealing the bonding of solvated Ru complexes with valence-to-core resonant inelastic X-ray scattering. *Chem. Sci.* **12**, 3713–3725 (2021).
195. Kim, J. et al. Excitonic quasiparticles in a spin–orbit Mott insulator. *Nat. Commun.* **5**, 4453 (2014).
196. Paris, E. et al. Strain engineering of the charge and spin–orbital interactions in Sr_2IrO_4. *Proc. Natl Acad. Sci. USA* **117**, 24764–24770 (2020).
197. Gretarsson, H. et al. Crystal-field splitting and correlation effect on the electronic structure of A(2)IrO(3). *Phys. Rev. Lett.* **110**, 076402 (2013).
198. Kim, J. et al. Large spin-wave energy gap in the bilayer iridate $Sr_3Ir_2O_7$: evidence for enhanced dipolar interactions near the Mott metal–insulator transition. *Phys. Rev. Lett.* **109**, 157402 (2012).
199. Yuan, B. et al. Determination of Hund's coupling in 5*d* oxides using resonant inelastic X-ray scattering. *Phys. Rev. B* **95**, 235114 (2017).
200. Ament, L. J. P., Khaliullin, G. & van den Brink, J. Theory of resonant inelastic X-ray scattering in iridium oxide compounds: probing spin–orbit-entangled ground states and excitations. *Phys. Rev. B* **84**, 020403 (2011).
201. Revelli, A. et al. Resonant inelastic x-ray incarnation of Young's double-slit experiment. *Sci. Adv.* **5**, 4020 (2019).
202. Lu, X. et al. Dispersive magnetic and electronic excitations in iridate perovskites probed by oxygen K-edge resonant inelastic X-ray scattering. *Phys. Rev. B* **97**, 041102 (2018).
203. Sala, M. M. et al. Orbital occupancies and the putative j_{eff}=1/2 ground state in Ba_2IrO_4: a combined oxygen *K*-edge XAS and RIXS study. *Phys. Rev. B* **89**, 121101(R) (2014).
204. Zimmermann, V. et al. Coherent propagation of spin–orbit excitons in a correlated metal. *npj Quantum Mater.* **8**, 53 (2023).
205. van Veenendaal, M., Carra, P. & Thole, B. T. X-ray resonant Raman scattering in the rare earths. *Phys. Rev. B* **54**, 16010–16023 (1996).
206. van Veenendaal, M. & Benoist, R. X-ray absorption and resonant inelastic X-ray scattering in the rare earths. *Phys. Rev. B* **58**, 3741–3749 (1998).
207. Butorin, S. M. Resonant inelastic X-ray scattering as a probe of optical scale excitations in strongly electron-correlated systems: quasi-localized view. *J. Electron. Spectros. Relat. Phenom.* **110**, 213–233 (2000).
208. Amorese, A. et al. Resonant inelastic X-ray scattering investigation of the crystal-field splitting of Sm^{3+} in SmB_6. *Phys. Rev. B* **100**, 241107 (2019).
209. Amorese, A. et al. Orbital selective coupling in $CeRh_3B_2$: coexistence of high Curie and high Kondo temperatures. *Phys. Rev. B* **107**, 115164 (2023).
210. Zatsepin, D. A. et al. Strong anisotropy of resonant inelastic X-ray scattering from charge-transfer excitations in UO_3. *J. Phys. Condens. Matter* **14**, 2541–2546 (2002).
211. Butorin, S. M. & Shuh, D. K. Electronic structure of americium sesquioxide probed by resonant inelastic X-ray scattering. *Phys. Rev. B* **108**, 195152 (2023).
212. Kvashnina, K. O. et al. Resonant inelastic X-ray scattering of curium oxide. *Phys. Rev. B* **75**, 115107 (2007).
213. Kvashnina, K. O. et al. Trends in the valence band electronic structures of mixed uranium oxides. *Chem. Commun.* **54**, 9757–9760 (2018).
214. Polly, R., Schacherl, B., Rothe, J. & Vitova, T. Relativistic multiconfigurational ab initio calculation of uranyl 3*d*4*f* resonant inelastic X-ray scattering. *Inorg. Chem.* **60**, 18764–18776 (2021).
215. Vitova, T. et al. The role of the 5*f* valence orbitals of early actinides in chemical bonding. *Nat. Commun.* **8**, 1–9 (2017).
216. Butorin, S. M. 3*d*-4*f* resonant inelastic X-ray scattering of actinide dioxides: crystal-field multiplet description. *Inorg. Chem.* **59**, 16251–16264 (2020).
217. Kvashnina, K. O., Walker, H. C., Magnani, N., Lander, G. H. & Caciuffo, R. Resonant X-ray spectroscopy of uranium intermetallics at the $M_{4,5}$ edges of uranium. *Phys. Rev. B* **95**, 245103 (2017).
218. Marino, A. et al. Singlet magnetism in intermetallic UGa_2 unveiled by inelastic X-ray scattering. *Phys. Rev. B* **108**, 045142 (2023).
219. Lander, G. H. et al. Resonant inelastic X-ray spectroscopy on UO_2 as a test case for actinide materials. *J. Phys. Condens. Matter* **33**, 06LT01 (2021).
220. Piancastelli, M. N. et al. Hard X-ray spectroscopy and dynamics of isolated atoms and molecules: a review. *Rep. Prog. Phys.* **83**, 016401 (2020).
221. Guillemin, R. et al. Angular and dynamical properties in resonant inelastic X-ray scattering: case study of chlorine-containing molecules. *Phys. Rev. A* **86**, 039903 (2012).
222. Püttner, R. et al. Si $1s^{-1}$, $2s^{-1}$ and $2p^{-1}$ lifetime broadening of SiX_4 (X=F, Cl, Br, CH3) molecules: SiF_4 anomalous behaviour reassessed. *Phys. Chem. Chem. Phys.* **21**, 8827–8836 (2019).
223. Marchenko, T. et al. Ultrafast nuclear dynamics in the doubly-core-ionized water molecule observed via Auger spectroscopy. *Phys. Rev. A* **98**, 063403 (2018).
224. Travnikova, O. et al. Subfemtosecond control of molecular fragmentation by hard X-ray photons. *Phys. Rev. Lett.* **118**, 213001 (2017).
225. Fohlisch, A. et al. Direct observation of electron dynamics in the attosecond domain. *Nature* **436**, 373–376 (2005).
226. Piancastelli, M. N. et al. Core-hole-clock spectroscopies in the tender X-ray domain. *J. Phys. B At. Mol. Opt. Phys.* **47**, 124031 (2014).
227. Marchenko, T. et al. Electron dynamics in the core-excited CS_2 molecule revealed through resonant inelastic X-ray scattering spectroscopy. *Phys. Rev. X* **5**, 031021 (2015).
228. Lundberg, M. et al. Metal-ligand covalency of iron complexes from high-resolution resonant inelastic X-ray scattering. *J. Am. Chem. Soc.* **135**, 17121–17134 (2013).
229. Braun, A. et al. X-ray spectroscopic study of the electronic structure of a trigonal high- spin Fe(IV)=O complex modeling non-heme enzyme intermediates and their reactivity. *J. Am. Chem. Soc.* **145**, 18977–18991 (2023).
230. Glatzel, P. et al. The electronic structure of Mn in oxides, coordination complexes, and the oxygen-evolving complex of photosystem II studied by resonant inelastic X-ray scattering. *J. Am. Chem. Soc.* **126**, 9946–9959 (2004).
231. Kroll, T. et al. Effect of 3*d*/4*p* mixing on 1*s*2*p* resonant inelastic X-ray scattering: electronic structure of oxo-bridged iron dimers. *J. Am. Chem. Soc.* **143**, 4569–4584 (2021).
232. Hall, E. R. et al. Valence-to-core-detected X-ray absorption spectroscopy: targeting ligand selectivity. *J. Am. Chem. Soc.* **136**, 10076–10084 (2014).
233. Gallo, E. et al. Preference towards five- coordination in Ti silicalite- 1 upon molecular adsorption. *ChemPhysChem* **14**, 79–83 (2013).
234. Glatzel, P. et al. In situ characterization of the 5d density of states of Pt nanoparticles upon adsorption of CO. *J. Am. Chem. Soc.* **132**, 2555–2557 (2010).
235. Kunnus, K. et al. Quantifying the steric effect on metal–ligand bonding in Fe carbene photosensitizers with Fe 2*p*3*d* resonant inelastic X-ray scattering. *Inorg. Chem.* **61**, 1961–1972 (2022).
236. House, R. A. et al. Covalency does not suppress O_2 formation in 4*d* and 5*d* Li-rich O-redox cathodes. *Nat. Commun.* **12**, 2975 (2021).
237. House, R. A. et al. First-cycle voltage hysteresis in Li-rich 3*d* cathodes associated with molecular O(2) trapped in the bulk. *Nat. Energy* **5**, 777–785 (2020).
238. House, R. A. et al. Delocalized electron holes on oxygen in a battery cathode. *Nat. Energy* **8**, 351–360 (2023).
239. House, R. A. et al. Superstructure control of first-cycle voltage hysteresis in oxygen-redox cathodes. *Nature* **577**, 502 (2020).
Resonant inelastic X-ray scattering application to battery systems showing molecular oxygen.
240. Wernet, P. et al. Orbital-specific mapping of the ligand exchange dynamics of Fe(CO)(5) in solution. *Nature* **520**, 78–81 (2015).
Time-resolved resonant inelastic X-ray scattering experiment.
241. Schreck, S. et al. Dynamics of the OH group and the electronic structure of liquid alcohols. *Struct. Dyn.* **1**, 054901 (2014).
242. Jay, R. M. et al. Tracking C–H activation with orbital resolution. *Science* **380**, 955–960 (2023).
243. Wang, R.-P. et al. Saturation and self-absorption effects in the angle-dependent 2*p*3*d* resonant inelastic X-ray scattering spectra of Co 3+. *J. Synchrotron Radiat.* **27**, 1–9 (2020).
244. Titus, C. J. et al. *L*-edge spectroscopy of dilute, radiation-sensitive systems using a transition-edge-sensor array. *J. Chem. Phys.* **147**, 214201 (2017).
245. Lee, S. J. et al. Soft X-ray spectroscopy with transition-edge sensors at Stanford Synchrotron Radiation Lightsource beamline 10-1. *Rev. Sci. Instrum.* **90**, 113101 (2019).
246. Vig, S. et al. Measurement of the dynamic charge response of materials using low- energy, momentum-resolved electron energy-loss spectroscopy (M-EELS). *SciPost Phys.* **3**, 026 (2017).
247. Higley, D. J. et al. Stimulated resonant inelastic X-ray scattering in a solid. *Commun. Phys.* **5**, 83 (2022).
248. Kroll, T. et al. Observation of seeded Mn Kβ stimulated X-ray emission using two-color X-ray free-electron laser pulses. *Phys. Rev. Lett.* **125**, 037404 (2020).
249. Bahrdt, J. et al. First observation of photons carrying orbital angular momentum in undulator radiation. *Phys. Rev. Lett.* **111**, 034801 (2013).
250. van Veenendaal, M. & McNulty, I. Prediction of strong dichroism induced by X rays carrying orbital momentum. *Phys. Rev. Lett.* **98**, 157401 (2007).
251. Elnaggar, H. et al. Noncollinear ordering of the orbital magnetic moments in magnetite. *Phys. Rev. Lett.* **123**, 207201 (2019).
252. Li, Z. X., Wang, Z. Y., Cao, Y. S. & Yan, P. Generation of twisted magnons via spin-to-orbital angular momentum conversion. *Phys. Rev. B* **105**, 174433 (2022).
253. Zhou, K. J., Matsuyama, S. & Strocov, V. N. *hν*(2)-concept breaks the photon-count limit of RIXS instrumentation. *J. Synchrotron Radiat.* **27**, 1235–1239 (2020).
254. Kokkonen, E. et al. Upgrade of the SPECIES beamline at the MAX IV laboratory. J. *Synchrotron Radiat.* **28**, 588–601 (2021).
255. Chiuzbaian, S. G. et al. Design and performance of AERHA, a high acceptance high resolution soft X-ray spectrometer. *Rev. Sci. Instrum.* **85**, 043108 (2014).
256. Boots, M., Muir, D. & Moewes, A. Optimizing and characterizing grating efficiency for a soft X-ray emission spectrometer. *J. Synchrotron Radiat.* **20**, 272–285 (2013).
257. Miyawaki, J. et al. A compact permanent-magnet system for measuring magnetic circular dichroism in resonant inelastic soft X-ray scattering. *J. Synchrotron Radiat.* **24**, 449–455 (2017).

258. Nowak, S. H. et al. A versatile Johansson-type tender X-ray emission spectrometer. *Rev. Sci. Instrum.* **91**, 033101 (2020).
259. Rovezzi, M. et al. TEXS: in-vacuum tender X-ray emission spectrometer with 11 Johansson crystal analyzers. *J. Synchrotron Radiat.* **27**, 813–826 (2020).
260. Glatzel, P. et al. The five-analyzer point-to-point scanning crystal spectrometer at ESRF ID26. *J. Synchrotron Radiat.* **28**, 362–ID371 (2021).
261. Ablett, J. M. et al. The GALAXIES inelastic hard X-ray scattering end-station at Synchrotron SOLEIL. *J. Synchrotron Radiat.* **26**, 263–271 (2019).
262. Weinhardt, L. et al. X-SPEC: a 70 eV to 15 keV undulator beamline for X-ray and electron spectroscopies. *J. Synchrotron Radiat.* **28**, 609–617 (2021).
263. Szlachetko, J. et al. In situ hard X-ray quick RIXS to probe dynamic changes in the electronic structure of functional materials. *J. Electron. Spectros. Relat. Phenom.* **188**, 161–165 (2013).
264. Cai, Y. Q. et al. Optical design and performance of the Taiwan inelastic X- ray scattering beamline (BL12XU) at SPRING- 8. *AIP Conf. Proc.* **705**, 340–343 (2004).
265. Alonso-Mori, R. et al. A multi-crystal wavelength dispersive X-ray spectrometer. *Rev. Sci. Instrum.* **83**, 073114 (2012).
266. Shvyd'ko, Y. V. et al. MERIX — next generation medium energy resolution inelastic X-ray scattering instrument at the APS. *J. Electron. Spectros. Relat. Phenom.* **188**, 140–149 (2013).
267. Glatzel, P. et al. Electronic structural changes of Mn in the oxygen-evolving complex of photosystem II during the catalytic cycle. *Inorg. Chem.* **52**, 5642–5644 (2013).